1996ApJ...463..570K

THE ASTROPHYSICAL JOURNAL, 463:570–592, 1996 June 1
© 1996. The American Astronomical Society. All rights reserved. Printed in U.S.A.

SYSTEMATIC EFFECTS ON DURATION MEASUREMENTS OF GAMMA-RAY BURSTS

THOMAS M. KOSHUT,[1,2] WILLIAM S. PACIESAS,[1,2] CHRYSSA KOUVELIOTOU,[2,3] JAN VAN PARADIJS,[1,4]
GEOFFREY N. PENDLETON,[1,2] GERALD J. FISHMAN,[5] AND CHARLES A. MEEGAN[5]
Received 1995 November 2; accepted 1995 December 13

ABSTRACT

The parameters T_{90} and T_{50} have recently been introduced as a measurement of the duration of gamma-ray bursts. We present here a description of the method of measuring T_{90} and T_{50} and its application to gamma-ray bursts observed with the Burst and Transient Source Experiment (BATSE) onboard the *Compton Gamma-Ray Observatory* (*CGRO*). We use simulated as well as observed time profiles to address some of the possible systematic effects affecting individual T_{90} (T_{50}) measurements. We show that these systematic effects do not mimic those effects that would result from time dilation if the burst sources are at distances of several Gpc. We discuss the impact of these systematic effects on the T_{90} (T_{50}) distributions for the gamma-ray bursts observed with BATSE. We distinguish between various types of T_{90} (T_{50}) distributions, and discuss the ways in which distributions observed with different experiments can vary, even though the measurements for commonly observed bursts may be the same. We then discuss the distributions observed with BATSE and compare them to those observed with other experiments.

Subject headings: gamma rays: bursts

1. INTRODUCTION

Since their discovery (Klebesadel, Strong, & Olson 1973), cosmic gamma-ray bursts (GRBs) have been the focus of observations made with numerous experiments. (For an extensive review of burst observations see Fishman & Meegan 1995). Due in large part to the lack of a distance scale, the origin of GRBs is still unknown. Developing detailed burst models is quite challenging when the intrinsic energy budget in gamma rays is uncertain by ~ 20 orders of magnitude. Burst models must therefore rely on the observations of a variety of burst properties for meaningful constraints.

Among the observed burst properties that can prove to be useful are the timescales over which these transient sources emit radiation. Many burst models (see Dar et al. 1992; Rees & Meszaros 1992; Usov 1992; Begelman et al. 1993; Meszaros & Rees 1993; Woosley 1993; and Katz 1994) make predictions that should be observable in a GRB time history. The burst time histories may be shaped on a number of timescales by either the emission process (e.g., through cooling timescales), the burst environment (through interaction with intervening matter, beaming effects, modulation by source rotation, the size of the emitting region), or even by the properties of space itself (in the case of cosmological models). In the past, a frequently used timescale has been the duration, which characterizes the time interval over which emission is observed above the background level.

The measurement of the duration of high-energy transients has historically been difficult. The measured durations of identical bursts emitted from identical sources located at very different distances could be substantially different, being affected by the signal-to-noise ratio of the observation. Comparing duration measurements between various experiments can be further complicated by differences in the sensitive energy ranges, integration timescales, and the local background flux (this will be addressed further in § 4).

We will discuss the use of two parameters, T_{90} and T_{50} (Kouveliotou et al. 1993), as measures of the characteristic timescale over which transient sources emit radiation (i.e., the "duration"). In § 2 we provide a definition of T_{90} (T_{50}), an extensive description of how these quantities are measured for GRBs observed with BATSE, and a discussion of their statistical uncertainties δT_{90} and δT_{50}. In § 3 we will explore the systematic effects associated with the measurement of T_{90} (T_{50}), using both simulated simple GRB time profiles, and observed burst profiles whose signal-to-noise ratios are varied. The methods used to simulate GRBs and to vary the signal-to-noise ratio of observed bursts are discussed in detail in this section. In § 4 we discuss T_{90} (T_{50}) distributions in general, and how they can vary between different experiments. We then briefly review the BATSE T_{90} (T_{50}) results, followed by a discussion of the impact of the systematic effects on these BATSE observations. We then review recent T_{90} and T_{50} measurements made with other experiments. Our concluding remarks are presented in § 5. Appendix A provides pertinent details about the BATSE instrumentation and data types. Appendix B discusses the details of the analytic calculations of T_{90} (T_{50}) for the simple time profile shapes used in our simulations.

2. T_{90} AND T_{50} AS MEASUREMENTS OF DURATION

2.1. *Definition of T_{90} and T_{50}*

T_{90} is defined as the time it takes to observe 90% of the total background-subtracted counts S_{tot} in a burst, starting and ending when 5% and 95% of S_{tot} have been observed, respectively. Similarly, T_{50} is defined as the time over which 50% of the counts S_{tot} has been observed, starting and ending when 25% and 75% of S_{tot}, respectively, have been observed. Clearly, T_{90} must always be greater than or equal to T_{50}.

[1] Department of Physics, University of Alabama in Huntsville, Huntsville, AL 35899.
[2] At NASA/Marshall Space Flight Centre, Huntsville, AL 35812.
[3] Universities Space Research Association, American City Building, Suite 212, Columbia, MD 21044
[4] Astronomical Institute "Anton Pannekoek," University of Amsterdam, Kruislaan 403, 1098 SJ Amsterdam, The Netherlands.
[5] NASA/Marshall Space Flight Center, Huntsville, AL 35812.

© American Astronomical Society • Provided by the NASA Astrophysics Data System

1996ApJ...463..570K

Let us represent a model source count rate history, summed over the entire observable energy range, as dS/dt. This model is assumed to be free of background. Throughout this work we will indicate differential elements with a lower-case d, while we will use the Greek symbol Δ to indicate discretely binned data, as in the observed count rates $\Delta C/\Delta t$. The total source counts observed from a given event are then given by

$$S_{\rm tot} = \int_{-\infty}^{\infty} \left(\frac{dS}{dt}\right) dt \ . \tag{1}$$

The function dS/dt is identically zero before the start time τ_s, and after the end time τ_e, of the transient emission from the source. Thus the limits of integration in equation (1) may be taken to be from τ_s to τ_e. We designate the time at which f% of the total source counts have been observed as τ_f; it is given by

$$\frac{f}{100} = \frac{\int_{\tau_s}^{\tau_f} (dS/dt)dt}{S_{\rm tot}} \ . \tag{2}$$

T_{90} is then given by

$$T_{90} = \tau_{95} - \tau_5 \tag{3}$$

and T_{50} is similarly given by

$$T_{50} = \tau_{75} - \tau_{25} \ . \tag{4}$$

T_{90} and T_{50} are theoretically independent of the burst signal-to-noise ratio S/N. The extent to which this is an idealization will be discussed extensively in § 3.

The parameter T_{90} is not equivalent to the duration T_d of a transient. The 10% of the total emission lying outside of the T_{90} interval may be weak and extended (as with time profiles that have a fast rise followed by a nearly exponential decay), causing a significant difference between the values of duration and T_{90}.

The duration can also differ from T_{90} by the way that the two quantities characterize events exhibiting temporal structures separated by extended periods with no observable emission above background. Figure 1 shows a GRB observed with BATSE in which there is a single pulse (containing less than 5% of the counts in the entire event) at the trigger time, followed by a much larger emission episode. The T_{90} interval was found to start at $\sim\tau_{\rm trg} + 108$ s and end at $\sim\tau_{\rm trg} + 138$ s, giving a T_{90} of ~ 30 s. However, by eye one would estimate the duration T_d to be ~ 140 s.

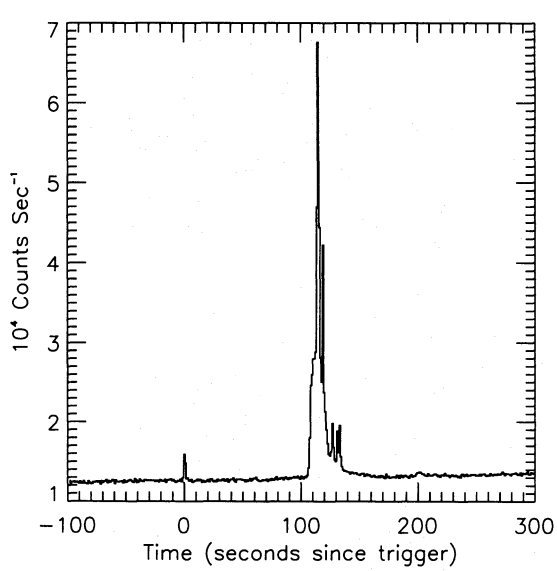

FIG. 1.—Time history of burst 1B 910522. A weak precursor at $t \approx 0$ s is found to contain less than 5% of the total counts in the event, thus being excluded from the T_{90} interval.

2.2. *Calculating T_{90} and T_{50} from the BATSE Data*

The BATSE data used for calculating T_{90} and T_{50} are the discriminator data from the Large Area Detectors (LADs) (the BATSE instrumentation and data types are briefly described in Appendix A; for more detailed information see Fishman et al. 1989 and Horack 1991). These include the DISCLA data, with a time resolution of 1.024 s, the PREB and DISCSC data, with a time resolution of 64 ms, and sometimes the TTE data, binned to a time resolution of 1 ms. Each of these data types consists of the count rates observed in the four LAD discriminator energy channels separately; all data used here are summed (either onboard or on the ground) over the triggered detectors.

For each burst, the data types are concatenated to span the time range from ~ 115 s prior to the burst trigger time $\tau_{\rm trg}$ to $\sim\tau_{\rm trg} + 360$ s during the early part of the mission (before 1992 December 17), and out to $\sim\tau_{\rm trg} + 550$ s afterward. Each time interval in this range is covered by the data type offering the finest time resolution available. Thus the concatenated data usually consist of DISCLA data from $\sim\tau_{\rm trg} - 115$ s to $\tau_{\rm trg} - 2$ s, PREB data from $\sim\tau_{\rm trg} - 2$ s to $\tau_{\rm trg}$, DISCSC data from $\tau_{\rm trg}$ to $\tau_{\rm trg} + 240(550)$ s, and during the early part of the mission the interval from $\sim\tau_{\rm trg} + 240$ s through $\tau_{\rm trg} + 360$ s is spanned by DISCLA data once again. The time range of the concatenated data can be extended in either direction using DISCLA data if the transient event displays either pretrigger emission, or emission that extends significantly later than $\tau_{\rm trg} + 240(550)$ s. If the event has a short duration (≤ 2 s), or if it contains a rapid rise in intensity near $t = \tau_{\rm trg}$, a short time interval near the trigger time may be covered by TTE data rather than PREB and DISCSC. The start and end times of this interval depend on the intensity of the burst (see Appendix A for more details), but this interval typically starts no earlier than $\tau_{\rm trg} - 0.18$ s and ends no later than $\sim\tau_{\rm trg} + 2$ s.

We designate the count rate observed in the ith energy channel during the jth time bin as $\Delta C(E_i, t_j)/\Delta t_j$, where Δt_j is the duration of the jth time bin. This indexing convention will be used for the remainder of this work. The omission of indices will imply that the entire range of that index should be considered. Figure 2*a* shows an example of a GRB time history, made using the concatenated data types, summed over all four BATSE energy channels ($\sim$20–2000 keV).

The background count rates, which we will represent as $dB(E, t)/dt$, in each of the four discriminator channels must be modeled before their subtraction from the observed count rates. Background models are created by using background time intervals during which the source is believed to be below the LAD detection threshold, fitting the observed data in these intervals to a polynomial of order p, and interpolating the fit across the source intervals. We used values of p between two and four; a different index is allowed for the background model in each channel. Any number of background intervals can be used, though one interval on each side of the event is often sufficient. When the burst consists of episodes of flux separated by large time intervals during which the source appears to be absent, it is some-

© American Astronomical Society • Provided by the NASA Astrophysics Data System

1996ApJ...463..570K

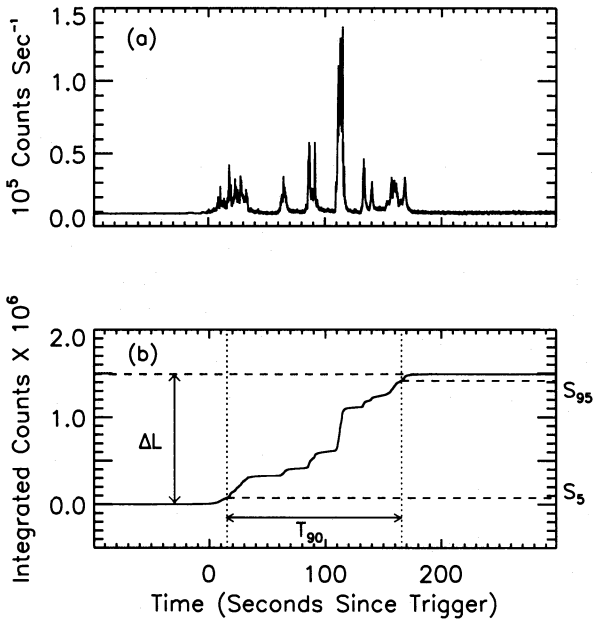

FIG. 2.—(*a*) Time profile using concatenated data types, summed over the energy range ~20–2000 keV, for burst 3B 940217. (*b*) A plot of the integrated counts as a function of time for the burst shown in (*a*), after the subtraction of a polynomial background model from the observed count rates.

times helpful to constrain the model fit by choosing a background interval during the quiescent period. It is important that the background intervals do not overlap with source emission. One should be particularly careful when the time history contains weak flux that is changing on a timescale similar to that of the orbital variation of the background rates. Background modeling is also critical for low-fluence events, where fluctuations in background may have fluences comparable to the total event fluence. In defining background intervals, we have also been careful to avoid time intervals during which the count rates contain contributions from an active discrete source exhibiting pulsed flux (such as Vela X-1) or X-ray flickering (as is often observed from the black hole candidate Cyg X-1), or when intensity steps due to occultation of a source by the limb of the Earth occur. It is also important not to contaminate background intervals with transient flux from unrelated GRBs, solar flares, or magnetospheric particle events.

The background model $\Delta B(E, t)/\Delta t$ is subtracted from the observed count rates $\Delta C(E, t)/\Delta t$ to give background-subtracted count rates $\Delta S(E, t)/\Delta t$ in each channel. The integrated source counts $S(t)$ observed during any time interval (t_a, t) is given by

$$S(t) = \sum_{j=t_a}^{t} \left[\frac{\Delta S(t_j)}{\Delta t_j}\right] \Delta t_j \,, \tag{5}$$

where $\Delta S(t)/\Delta t$ represents the background-subtracted count rates summed over all discriminator channels and j is a time bin index. We compute the integrated counts as a function of time over a user-defined time interval (t_{j1}, t_{j2}), where t_{j1} is chosen before the start of the event and t_{j2} is chosen after the end of the event. As an example, the solid curve in Figure 2*b* shows the integrated counts (summed over all four energy channels, with $t_{j1} = -100$ s and $t_{j2} = 300$ s) as a function of time for the burst in Figure 2*a*. Note that the data must be complete over the interval (t_{j1}, t_{j2}); $S(t)$ given by equation (5) is unknown for all times after any missing data. Thus, T_{90} (T_{50}) cannot be calculated for any event during which there is a data gap.

If our background model were perfectly accurate, then the solid curve in Figure 2*b* would remain flat from the first point until the first detection of source emission. This time interval, immediately preceding the onset of the burst emission, will hereafter be referred to as the zero-fluence interval. As burst emission is detected, the slope at any point on this curve indicates the intensity of the burst. The curve would ultimately return to a line with a slope of zero, indicating the cessation of emission from the source. The time interval following the last detected source emission will hereafter be referred to as the total-fluence interval.

Theoretically, negative slopes in Figure 2*b* are not possible; however, in practice negative slopes result from discrepancies between our background model and the true background count rates. These discrepancies may occur over long timescales due to the observed background rates varying faster than variations allowed by our low-order polynomial models (for example, when the spacecraft is in the proximity of the South Atlantic Anomaly), or they may occur over short timescales, due to Poisson fluctuations in the counting rates.

The start and end times of the zero-fluence and total-fluence intervals are manually defined; these intervals should not overlap with any source emission. The zero-fluence level L_z, and the total-fluence level L_t, represent the value of the integrated counts $S(t)$ immediately prior to the onset of the source emission, and immediately after the cessation of the source emission, respectively. L_z and L_t are found by calculating the mean value of $S(t)$ during the user-defined zero-fluence and total-fluence intervals, respectively. The first time at which the integrated counts $S(t)$ exceeds L_z (L_t) is considered the start (end) time of burst emission. The spreads of the data about the mean in the zero-fluence and total-fluence intervals are characterized by their variances $(dL_z)^2$ and $(dL_t)^2$, respectively.

The total number of counts ΔL observed due to the GRB is then

$$\Delta L = L_t - L_z \,, \tag{6}$$

and the f% fluence level, S_f, is given by

$$S_f = L_z + \frac{f}{100}\,\Delta L \,. \tag{7}$$

S_f represents the value of the integrated counts $S(t)$ when f% of the total source counts have been detected. The time at which the integrated counts reaches the value S_f can then be found and designated as τ_f. The true value of τ_f can fall anywhere within a data bin. When the appropriate data bin in which τ_f is contained has been found, then the value assigned to τ_f is the start time of that bin if f is either 5 or 25, or the end time of that bin if f is either 75 or 95. The values of T_{90} (T_{50}) are then found from equations (3) and (4).

2.3. *Statistical Uncertainties in T_{90} and T_{50}*

The uncertainties in S_f, $(dS_f)_{\rm tot}$, consist of contributions from two components: $(dS_f)_{\rm cnt}$, due to the uncertainty in the integrated counts $S(t)$ at any time t caused by detector counting statistics, and $(dS_f)_{\rm fluc}$, due to the uncertainty in the levels L_z and L_t caused by statistical fluctuations about the smooth background model. The uncertainty $(dS_f)_{\rm tot}$ is

© American Astronomical Society • Provided by the NASA Astrophysics Data System

1996ApJ...463..570K

given by

$$(dS_f)_{\rm tot} = \sqrt{[(dS_f)_{\rm cnt}]^2 + [(dS_f)_{\rm fluc}]^2} \,. \quad (8)$$

Assuming no uncertainties in our background model $\Delta B(E, t)/\Delta t$, the uncertainties $(\delta S/\delta t)_j$ in the background-subtracted count rates $\Delta S(E, t)/\Delta t$ and the uncertainties $(\delta C/\delta t)_j$ in the observed count rates $\Delta C(E, t)/\Delta t$ are equivalent. If we represent the observed count rates in time bin j, summed over the four energy channels, as $\Delta C(t_j)/\Delta t_j$, the uncertainty $(dS_f)_{\rm cnt}$ is then given by

$$(dS_f)^2_{\rm cnt} = \sum_{j=\tau_0}^{\tau_f} \left[\frac{\Delta C(t_j)}{\Delta t_j}\right] \Delta t_j \,, \quad (9)$$

where τ_0 is the time at which the integrated counts exceed the level L_z.

From equations (6) and (7), the 5% fluence level S_5 can be written as

$$S_5 = \frac{19L_z + L_t}{20} \,. \quad (10)$$

The uncertainty $(dS_5)_{\rm fluc}$ in S_5 is given by

$$(dS_5)_{\rm fluc} = \sqrt{\left(\frac{\partial S_5}{\partial L_z}\right)^2 dL_z^2 + \left(\frac{\partial S_5}{\partial L_t}\right)^2 dL_t^2} \,, \quad (11)$$

where dL_z and dL_t are the variances associated with L_z and L_t, and the partial derivatives are found analytically from equation (10) to be $\partial S_5/\partial L_z = 0.95$ and $\partial S_5/\partial L_t = 0.05$. Equation (11) becomes

$$(dS_5)_{\rm fluc} = \sqrt{(0.95)^2\, dL_z^2 + (0.05)^2\, dL_t^2} \,. \quad (12)$$

Similarly, we find

$$S_{95} = \frac{L_z + 19L_t}{20} \quad (13)$$

and

$$(dS_{95})_{\rm fluc} = \sqrt{(0.05)^2\, dL_z^2 + (0.95)^2\, dL_t^2} \,. \quad (14)$$

The uncertainties $(dS_5)_{\rm tot}$ and $(dS_{95})_{\rm tot}$ can now be found using equations (8) and (9).

The times τ_{f-} and τ_{f+} are the times at which $S_f - (dS_f)_{\rm tot}$ and $S_f + (dS_f)_{\rm tot}$ counts, respectively, have been detected. We define $\Delta\tau_f$ as

$$\Delta\tau_f = \tau_{f+} - \tau_{f-} \,. \quad (15)$$

The statistical uncertainty δT_{90} in T_{90} is now calculated by

$$\delta T_{90} = \sqrt{(\Delta\tau_5)^2 + (\Delta\tau_{95})^2} \,. \quad (16)$$

It is through the quantities $\Delta\tau_5$ and $\Delta\tau_{95}$ that the dependence of δT_{90} on the detailed shape of the burst time profile is introduced. The error δT_{50} in T_{50} is computed similarly.

Note that the minimum value of $\Delta\tau_f$ that can be achieved is $t_{\rm res}$, where $t_{\rm res}$ is the time resolution of the discrete data at the time τ_f. Assuming that the values of τ_f fall within data bins of equal time resolution $t_{\rm res}$, the minimum value of the uncertainties δT_{90} and δT_{50} given by equation (16) is $t_{\rm res}(2)^{1/2}$.

The method used to calculate the statistical uncertainties δT_{90} and δT_{50} in the BATSE 1B (Fishman et al. 1994), 2B (Meegan et al. 1994), and 3B catalogs (Meegan et al. 1995) did not include the contribution of $(dS_f)_{\rm cnt}$ to $(dS_f)_{\rm tot}$. This effect is insignificant for short events, where the sum in equation (9) contains a small number of terms. After recalculating the uncertainties for a number of bursts, we estimate that the statistical uncertainties δT_{90} and δT_{50} for long-duration bursts in these three BATSE catalogs should be larger by a factor of ~ 1.5.

2.4. *Comparison of T_{90} and T_{50}*

Some believe that T_{50} is a better measure of burst duration than T_{90}, because it is less susceptible to weak flux in the wings of the burst (Kargatis et al. 1994). This statement is correct only under the assumption that weak flux preferentially occurs near the start and end of the burst, and avoids the intermediate region of the burst where τ_{25} and τ_{75} are likely to be found. Both T_{90} and T_{50} are susceptible to weak flux, and which is affected more depends entirely on the detailed profile shape. Similarly, T_{90} is not necessarily more sensitive than T_{50} to precursor emission separated from the main burst emission by an extended background interval, unless one assumes a priori that the flux is more intense at $t = \tau_{25}$ than at $t = \tau_5$. By examination of Figure 2*b*, it is apparent that if the first 5% of the counts observed from the burst were removed, the resulting effect on the values of τ_f is dependent on the shape of the time profile.

To investigate this issue further, we examined the distribution of the relative uncertainties δT_{90} and δT_{50} in the BATSE 2B catalog, shown in Figures 3*a* and 3*b*, respectively. The two distributions are very similar, thus not lending support to a preference of one measure over the other. The average percentage uncertainties are $\langle \delta T_{90} \rangle = 19 \pm 2.2$ (36)% and $\langle \delta T_{50} \rangle = 16 \pm 1.5$ (24)%, where the first error indicates our uncertainty in the mean and the error in parentheses is the sample standard deviation and characterizes the width of the distribution. The majority of the large percentage uncertainties occur at small values of T_{90} (T_{50}), and are the result of the finite time resolution of the binned data. Not all BATSE measurements of small T_{90} (T_{50}) have large percentage uncertainties. Recall that BATSE observations of bursts often include TTE data (see Appendix A) which are used at a time resolution of 1 ms. For those bursts covered entirely by TTE rather than the coarser DISCSC, the minimum uncertainty in T_{90} (T_{50}) (given by eq. [16]) drops from ~ 0.091 s to ~ 1.4 ms.

2.5. *Other Quantities*

Hardness ratios, which roughly characterize the source spectrum, can be obtained from the total counts detected in each energy channel during the T_{90} (T_{50}) interval (with the interval determined as just described from the rates summed over all energy channels). These hardness ratios were calculated for the BATSE data and were used to confirm that on average short bursts have harder spectra than longer bursts (Kouveliotou et al. 1993).

Two other quantities which may be found are T_r and $T_{\rm dcy}$, which characterize the time required for the event to rise to peak intensity and to decay from peak intensity, respectively. The time $\tau_{\rm pk}$ is the time at which the background-subracted count rate, summed over all energy channels, is maximal. The time T_r to rise from the start of the T_{90} interval to peak intensity is then given by

$$T_r \equiv \tau_{\rm pk} - \tau_5 \,. \quad (17)$$

Similarly, the time $T_{\rm dcy}$ to decay from the peak intensity to

© American Astronomical Society • Provided by the NASA Astrophysics Data System

1996ApJ...463..570K

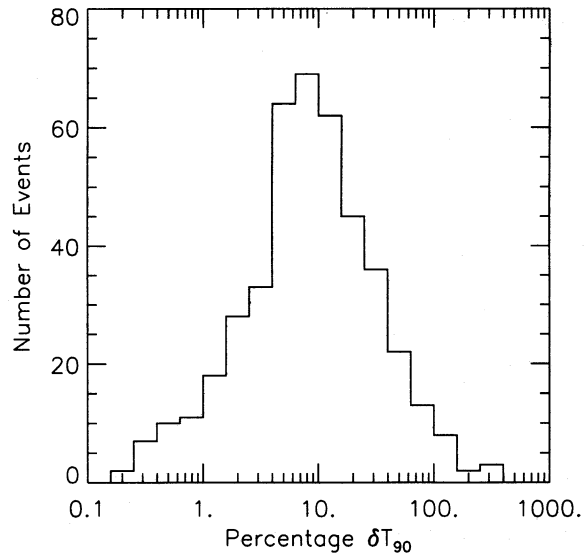

FIG. 3*a*

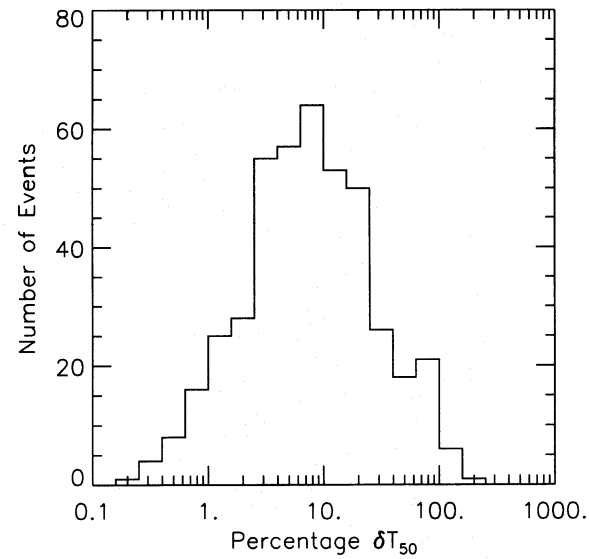

FIG. 3*b*

FIG. 3.—(*a*) The distribution of the percentage uncertainties in T_{90} for the bursts in the BATSE 2B catalog. (*b*) The distribution of the percentage uncertainties in T_{50} for the same sample.

the end of the T_{90} interval is given by

$$T_{\rm dcy} \equiv \tau_{95} - \tau_{\rm pk} \,. \tag{18}$$

These quantities are different from the usual rise and decay times which measure the times to rise from, and decay back to, the background count rate. Notice that it is possible for either T_r or $T_{\rm dcy}$ (though not both) to be negative, indicating that the peak intensity of the burst occurred either before τ_5 or after τ_{95}, respectively.

One can define a parameter $\lambda_{\rm pk}$, which characterizes the position of the peak intensity within an event, as

$$\lambda_{\rm pk} \equiv \frac{T_r}{T_{90}} \,. \tag{19}$$

If one accounts for negative values of T_r by setting them equal to zero, the value of $\lambda_{\rm pk}$ is constrained to fall within the range $0 \le \lambda_{\rm pk} < 1$. This parameter provides a sense of the asymmetry of the overall time history. If the peak intensity of the event is equally likely to occur at any time within the event, we would expect an average value $\langle\lambda_{\rm pk}\rangle \approx 0.5$, with an associated uncertainty that is due to a finite sample size.

3. SYSTEMATIC EFFECTS ON T_{90} AND T_{50}

In this section we explore some likely sources of systematic errors using simulated time profiles, and observed time profiles whose signal-to-noise ratios are varied. The simulated time profiles can be represented by simple formulae, and their values of T_{90} (T_{50}) can be calculated analytically. We verify that the code used to calculate T_{90} (T_{50}) works properly, by applying it to simulated noise-free burst profiles. We examine the effects of source intensity and background modeling on T_{90} (T_{50}) for simulated bursts with statistical noise. We then systematically reduce the signal-to-noise ratio of several observed bursts, and examine the dependence of T_{90} (T_{50}) on the detailed shape of the time profile as well as its intensity.

3.1. *Simulation of Simple Time Profiles*

The simulated data consisted of count rates $\Delta C(E, t)/\Delta t$ as a function of time, in each of the four BATSE discriminator energy channels, with a time resolution identical to that of the concatenated data described in § 2.2.

We first created background model count rates $\Delta B(E, t)/\Delta t$ in each of the four energy channels, by randomly selecting a set of polynomial coefficients from those used to model background in the T_{90} calculations of the 2B catalog. These coefficients were then used for the analyses discussed in §§ 3.1.1 and 3.1.2 (the effect of using different background models is considered in § 3.1.3). The only variations in this background model are long-term and are due to the orbital motion of the *CGRO* about the Earth. Statistical fluctuations in the count rates have not yet been added.

To simulate the source count rates $\Delta S(E, t)/\Delta t$ we first had to determine how to divide the total counts observed at any given time between the four discriminator energy channels. To accomplish this, we used a 2B catalog database consisting of the total counts observed in each energy channel during the T_{50} time interval. We neglect in this work the systematic effects on T_{90} (T_{50}) that may be introduced by varying spectral shapes; therefore, one count spectrum (shown in Fig. 4) was randomly selected from the 2B catalog and it was used for all of the burst time profile simulations. The shape of the count spectrum remains constant throughout each simulated burst; no spectral evolution is allowed.

We simulated three simple burst profile shapes: triangular, rectangular, and one exhibiting a fast rise followed by a nearly exponential decay (hereafter referred to as a FRED). These three forms were chosen because each could be described in a straightforward manner by a simple analytic expression, which allowed for their values of T_{90} and T_{50} to be calculated analytically.

The analytic model $(dS/dt)_i$ of a triangular time history in each energy channel may be written as

$$\left(\frac{dS}{dt}\right)_i = \begin{cases} 0\,, & t < \tau_s\,, \\ m_i t + b_i\,, & \tau_s \le t < \tau_{\rm pk}\,, \\ n_i t + d_i\,, & \tau_{\rm pk} \le t \le \tau_e\,, \\ 0\,, & t > \tau_e\,, \end{cases} \tag{20}$$

© American Astronomical Society • Provided by the NASA Astrophysics Data System

1996ApJ...463..570K

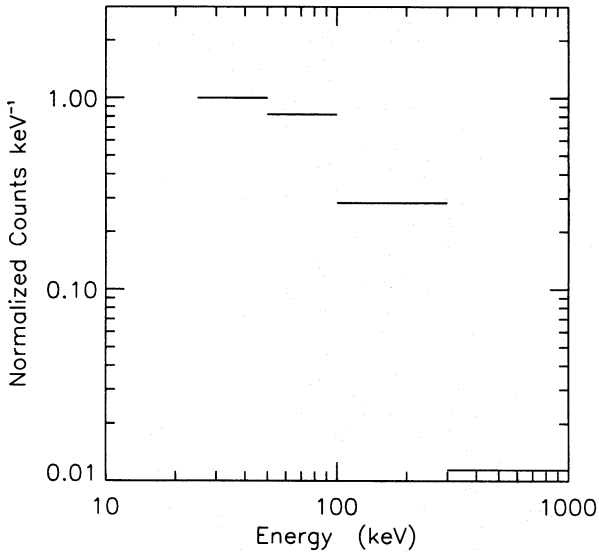

FIG. 4.—Count spectrum of BATSE burst 1B 911129, integrated over the T_{50} interval; this spectrum was used in the simulations of burst time profiles. All values are normalized to the value observed in the first energy channel (20–50 keV).

where τ_s is the start time of the source emission, τ_{pk} is the time of the peak emission, and τ_e is the end time of the source emission. Each of these three time constants are input in seconds relative to $t = 0$, and are independent of energy channel, for each simulation. The slopes m_i and n_i of the burst rise and decay are given by

$$m_i = \frac{P_i}{\tau_{pk} - \tau_s} \quad \text{and} \quad n_i = -\left(\frac{P_i}{\tau_e - \tau_{pk}}\right), \tag{21}$$

where P_i is the peak count rate in energy channel i. The constants b_i and d_i are given by

$$b_i = -\tau_s m_i \quad \text{and} \quad d_i = -\tau_e n_i \,. \tag{22}$$

Note that the energy dependence of equation (20) is entirely through the peak count rate P_i in each energy channel.

The analytic model of a simulated rectangular time history in energy chanel i may be written as

$$\left(\frac{dS}{dt}\right)_i = \begin{cases} 0\,, & t < \tau_s\,, \\ P_i\,, & \tau_s \le t < \tau_e\,, \\ 0\,, & t > \tau_e\,, \end{cases} \tag{23}$$

where τ_s and τ_e have the same meanings as before. As with the triangular profile, the energy dependence is provided through the peak count rate P_i in energy channel i.

Our FRED profile is an idealization of a subclass of bursts that are actually observed in the data set (Kouveliotou et al. 1991). The analytic expression for the model used to simulate a FRED in energy channel i is given by

$$\left(\frac{dS}{dt}\right)_i = \begin{cases} 0\,, & t < \tau_s\,, \\ P_i e^{-kt}\,, & t \ge \tau_s\,, \end{cases} \tag{24}$$

where τ_s is the start time of the emission, τ_d is the $1/e$ decay time, and $k = \tau_d^{-1}$. As before, P_i provides the energy dependence. Our simulated FREDs differ from those observed in the BATSE data set in that the observed bursts do not usually rise so rapidly to their peak intensity, and the decay of the observed bursts is seldom precisely exponential.

The final parameter of equations (20) through (24) that needs to be determined is the peak count rate P_i in energy channel i. The quantity used to characterize the burst intensity is the signal-to-noise ratio S/N at the peak of the time history summed over the energy channels 2 and 3. Using the background model we calculate the background counts $(B_{pk})_{2+3}$, summed over channels 2 and 3, observed at the peak, and the "noise" σ_{2+3} at the peak time, given by $[(B_{pk})_{2+3}]^{1/2}$. The source counts $(N_{pk})_{2+3}$ at the peak, summed over channels 2 and 3, corresponding to an input S/N is then given by

$$(N_{pk})_{2+3} = (\mathrm{S/N})\sigma_{2+3}\,. \tag{25}$$

These $(N_{pk})_{2+3}$ counts must be divided between channels 2 and 3 according to the previously selected count spectrum. Using the counts in these two channels and the assumed count spectrum, the peak count rate P_i in energy channel i is straightforwardly determined.

With the peak count rate P_i determined in each energy channel, and each of the appropriate time constants defined, the source count rates $\Delta S(E, t)/\Delta t$ in each channel are then calculated according to equation (20), equation (23), or equation (24). The total observed count rates $\Delta C'(E, t)/\Delta t$ are then determined by summing together the background model count rates and the source count rates,

$$\frac{\Delta C'(E, t)}{\Delta t} = \frac{\Delta B(E, t)}{\Delta t} + \frac{\Delta S(E, t)}{\Delta t}\,, \tag{26}$$

where the primed notation indicates that no statistical noise has been added to these rates. Therefore at this point the input signal-to-noise ratio S/N does not yet have its usual meaning, and has only been used as a measure of the burst intensity above a smooth background model. However, these rates can be very useful in testing the T_{90} (T_{50}) software (see § 3.1.1).

The final step in the simulation of the simple burst profiles $\Delta C(E, t)/\Delta t$ is to add statistical noise to the count rates $\Delta C'(E, t)/\Delta t$ in each energy channel. The number of counts ΔC in the jth time bin with noise added is given by

$$\Delta C_j = \Delta C'_j + \Delta\psi_j\,, \tag{27}$$

where $\Delta\psi_j$ represents the statistical noise and is randomly generated from a Gaussian distribution with a mean $\mu = \Delta C_j'$. The S/N now has its traditional meaning, and is more than just a measure of the burst intensity. The total count rates $\Delta C(E, t)/\Delta t$ in each energy channel are then given by

$$\frac{\Delta C(E, t)}{\Delta t} = \frac{\Delta B(E, t)}{\Delta t} + \frac{\Delta S(E, t)}{\Delta t} + \frac{\Delta\psi(E, t)}{\Delta t}\,. \tag{28}$$

After each simulation we checked whether the burst would have set the BATSE burst trigger on at least one of the three trigger timescales, under the assumption that the burst was observed in two LADs, with equal intensity in each detector (see Appendix A).

Figure 5 shows three sample simulated bursts with a background model and statistical noise added. Figure 5*a* is an example of a triangular burst, with S/N = 50 σ at the peak, and duration $T_d = \tau_e - \tau_s = 30$ s. Figure 5*b* shows an example of a rectangular burst, with S/N = 5.5 σ and a duration $T_d = 1.5$ s. Figure 5*c* shows an example of a FRED, with S/N = 15 σ and a decay time $\tau_d = 70$ s.

© American Astronomical Society • Provided by the NASA Astrophysics Data System

1996ApJ...463..570K

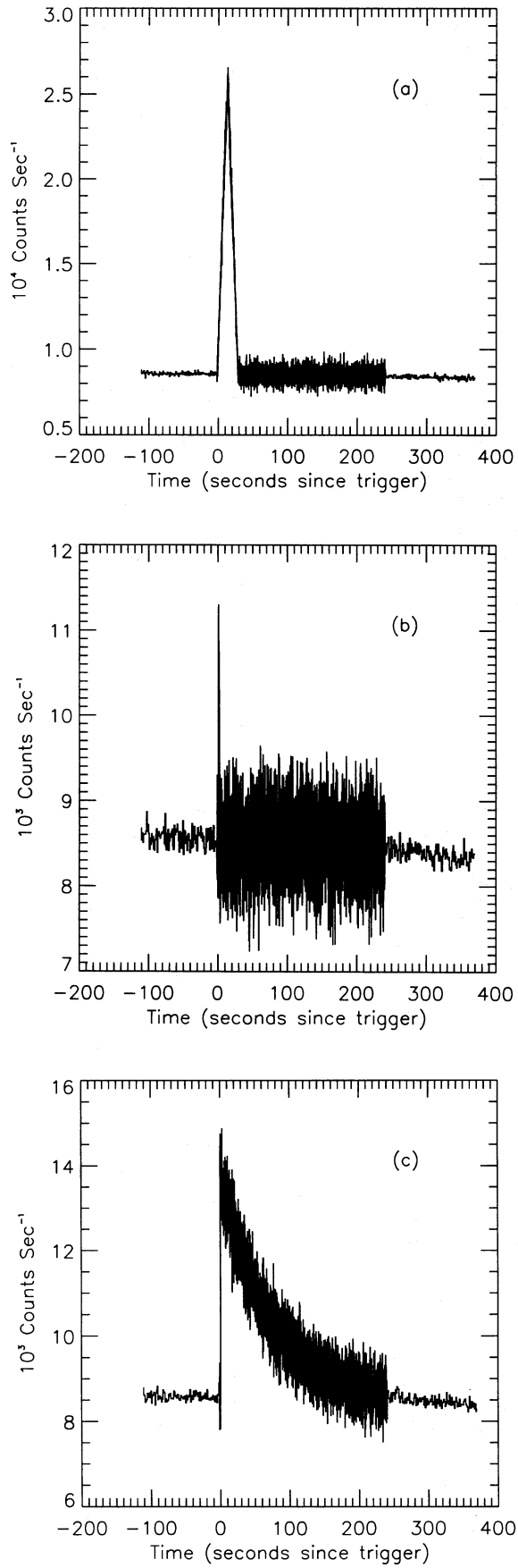

FIG. 5.—Examples of simulated burst time histories, with a background model and statistical noise added. (*a*) Triangular burst. (*b*) Rectangular burst. (*c*) Burst with a fast-rise and an exponential decay (FRED).

3.1.1. *Using Simulated Time Profiles to Test the T_{90} Code*

We used the procedure described in §§ 2.2 and 2.3 to calculate T_{90} (T_{50}) for a series of simulated bursts which were free of statistical noise. We then analytically calculated T_{90} (T_{50}) for each of these simulated bursts (these calculations are described in Appendix B). Nine simulations were run for each of three simple time profile shapes: triangular, rectangular, and FRED. The nine simulations included bursts with durations T_d of 1.5, 30, and 150 s (or decay times τ_d of 1.5, 30, and 70 s in the case of FRED profiles). For each of these profiles we assumed three different intensities (S/N): weak (5.5 σ), moderate (15 σ), and strong (50 σ). The signal-to-noise ratio S/N is still defined by equation (25); though noise has not been added to these profiles, σ_{2+3} can still be calculated. These signal-to-noise ratios do not have their traditional meaning; they are simply measures of the burst peak intensity.

The results of these simulations are given in Table 1, in the form of the largest relative error (E_R) as compared to the analytic values. Statistical uncertainties on the measured values cannot be calculated for these simulations due to the lack of statistical noise in the time profiles.

We see from Table 1 that significant errors occur for profiles with very short durations. These errors occur because the BATSE time histories consist of discretely sampled data while the analytic calculations are done using continuous functions. The measured values differ from the analytic values by less than one data bin. This is why the percentage errors increase as T_d decreases. This also explains why the percentage uncertainties in T_{50} are larger than those in T_{90}; T_{50} is always smaller than T_{90} and therefore is more susceptible to binning effects.

For each triangular burst of the same duration, the three measured values of T_{90} were identical, independent of the burst intensity. The same was true for the measured values of T_{50}. This was also true for the rectangular bursts. In each case the measured values of T_{90} and T_{50} for the triangular bursts were larger than the analytic values. The three measured values of T_{90} for the rectangular bursts with $T_d = 1.5$ s were lower than the analytic values; all other values of T_{90} and T_{50} for the rectangular bursts were larger than the analytic values. For the short FREDs, all values of T_{90} and T_{50} were larger than the analytic values, but by less than 5% and 2%, respectively. For these shorter FREDs, the values measured for T_{90} and T_{50} were independent of the burst intensity.

The results from the simulations of FREDs with longer decay times are indicative of the difficulty of making the measurements when the burst flux varies on timescales similar to those over which the background model is varying. Figures 6*a* and 6*b* show the measured values of T_{90} and T_{50}, respectively, as a function of the simulated burst intensity for FREDs with $\tau_d = 30$ s. The dashed lines indicate the known analytic values. It is clear that T_{90} and T_{50} show no systematic dependence on the burst intensity; however, the measured values of T_{90} and T_{50} are systematically lower than the analytic values by $\sim$2% and $\sim$1%, respectively.

The systematic errors are especially pronounced in the measured T_{90} and T_{50} values of the simulated FRED profiles with τ_d of 70 s (see Figs. 6*c* and 6*d*). We attribute these systematic errors to inadequate modeling of the background rates, largely due to the fact that the tail of the decay

© American Astronomical Society • Provided by the NASA Astrophysics Data System

1996ApJ...463..570K

TABLE 1

SIMULATION RESULTS FOR NOISE-FREE-PROFILES

Triangular			Rectangular		FRED		
T_d (s)	T_{90} E_R (%)	T_{50} E_R (%)	T_{90} E_R (%)	T_{50} E_R (%)	τ_d (s)	T_{90} E_R (%)	T_{50} E_R (%)
1.5	<7	<17	<1	<12	1.5	<5	<2
30	<1	<2	<1	<1	30	<2	<1
150.....	<1	<2	<1	<1	70	<18	<10

in intensity of the FRED is varying on the same timescale as are the background rates, and it is then very difficult to separate the two (even in this noise-free case). However, we do not find any systematic dependence of either T_{90} or T_{50} on the burst intensity. The systematic effects of background modeling and the detailed background model on T_{90} (T_{50}) will be addressed in § 3.1.3.

We would like to point out that the simulated triangular burst with $T_d = 150$ s and S/N = 5.5 would not have triggered the BATSE instrument. Therefore it was not included in Table 1. It will be seen in § 3.1.2 that when we simulated the same burst with statistical noise added, we found that the instrument would have triggered.

Using noise-free GRB simulations, we find that the primary sources of error in these measurements are the finite width of the discretely sampled data and the uncertainty in background modeling; the first error is unavoidable, and the second is examined in greater detail in § 3.1.3.

3.1.2. *Dependence of T_{90} on Signal-to-Noise Ratio*

We use the standard BATSE software to calculate T_{90} (T_{50}) for a series of simulated bursts which now contain statistical noise. Fifteen simulations were run for each of the three simple time profile shapes. The 15 simulations included bursts with durations T_d of 1.5, 30, and 150 s (or decay times τ_d of 1.5, 30, and 70 s for FRED profiles). For each duration, profiles of five values of S/N were simulated: 5.5, 10, 15, 30, and 50 σ. In these simulations, the signal-to-noise ratio has its traditional meaning. The results of these simulations are given in Table 2, in the form of the largest relative error (E_R) and the largest absolute deviation E_A from the analytic value. We note that for each burst profile, the size of the uncertainties δT_{90} (δT_{50}) was inversely proportional to the burst S/N.

For the triangular and rectangular bursts, measured values of T_{90} (T_{50}) that were less than the analytic values

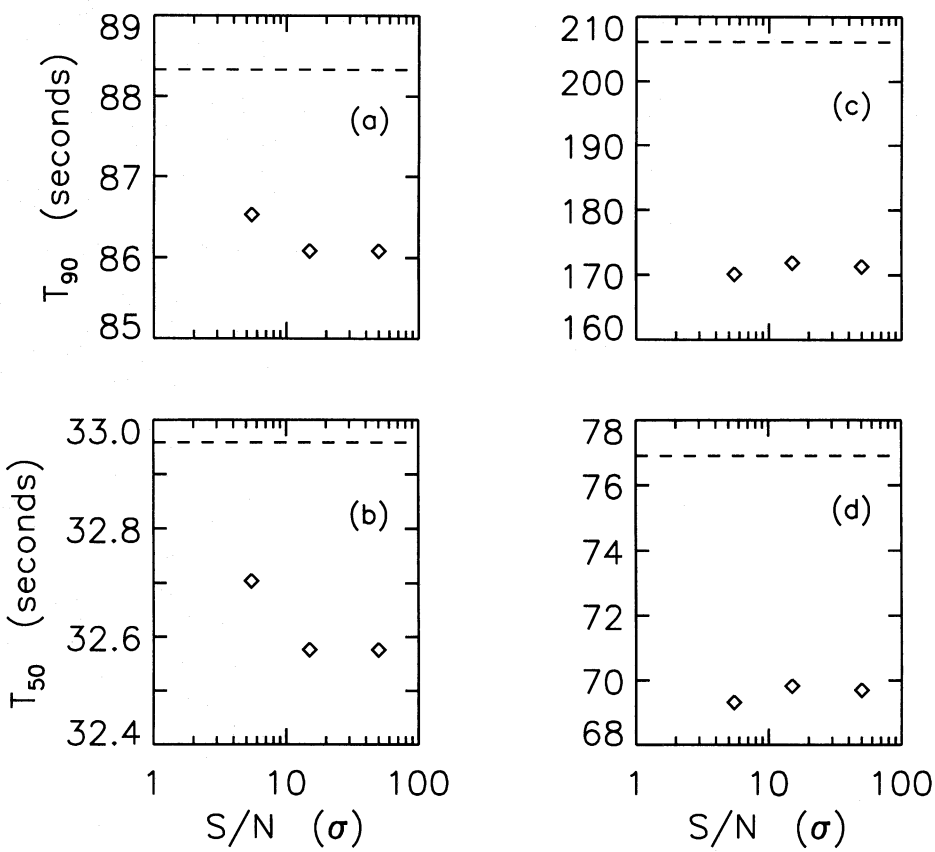

FIG. 6.—(*a*)–(*d*) The measured values of T_{90} and T_{50} as a function of burst S/N for simulated noise-free FRED time profiles. The dashed lines indicate the analytically calculated values of T_{90} and T_{50}. (*a*) $\tau_d = 30$ s, (*c*) $\tau_d = 70$ s.

© American Astronomical Society • Provided by the NASA Astrophysics Data System

1996ApJ...463..570K

were observed, but on average the measured values were larger. In no case did we find evidence for any systematic dependence of either T_{90} or T_{50} on the burst S/N. We find no evidence in the FRED case of $\tau_d = 1.5$ s for any dependence of either T_{90} or T_{50} on the burst S/N.

We find that the largest errors are associated with the longer duration FRED profiles (see Figs. 7*a* and 7*b*). For these FREDs with $\tau_d = 30$ s, the errors in T_{90} and T_{50} were les than 20% and 10%, respectively. The measured values are on average underestimated; however they are consistent with no systematic dependence of T_{90} or T_{50} on the burst S/N.

The systematic errors are pronounced in the measured T_{90} and T_{50} values of the simulated FRED profiles with $\tau_d = 70$ s (see Figs. 7*c* and 7*d*). A systematic dependence of T_{90} and T_{50} on the burst S/N is apparent, the bursts with smaller S/N having larger deviations of T_{90} and T_{50} from their analytic values. We will show in § 3.1.3 that this systematic dependence on burst S/N can be attributed to the inadequate modeling of the background rates.

If T_{90} (T_{50}) were systematically dependent on the burst S/N, then one would expect a tendency for the measured values to be consistently overestimated or underestimated in the weak case (S/N = 5.5 σ) for all profile shapes. The values of T_{90} and T_{50} for the weak triangular bursts were overestimated. There was no tendency for either underestimation or overestimation of T_{90} (T_{50}) for the weak rectangular bursts. T_{90} (T_{50}) were underestimated in the cases of the weak FRED bursts, except for the case of $\tau_d = 1.5$ s; however, we attribute this underestimation to incorrect background modeling. Thus, we conclude that any systematic variations of T_{90} (T_{50}) with burst S/N depend on the shape of the burst time profile.

We point out that in the case of one simulated triangular burst, that with T_d of 1.5 s and a S/N of 30, the uncertainty δT_{90} in the measured value of T_{90} was large, given by $T_{90} = 1.1 \pm 9.7$. This is due to the chance superposition of positive statistical fluctuations in the count rates in energy channels 1, 2, and 3. When the counts in these fluctuations were summed, they resulted in a large value of τ_{95+} (defined in § 2.3), thus a large value of $\Delta\tau_{95}$ given by equation (15), and consequently a large uncertainty δT_{90}. This is an indication that the value of the total fluence level L_t (see § 2.2) was not well determined. This illustrates the fact that the total counts in background fluctuations can be significant, compared to the total counts observed in short bursts, and can result in large statistical errors on measurements of T_{90} (T_{50}) for these bursts.

We also notice that unlike the simulated noise-free burst with S/N of 5.5 and T_d of 150 s, the same simulated burst profile with statistical noise added would have triggered the BATSE instrument.

3.1.3. *Dependence of T_{90} on Background Effects*

The effects of inadequate background modeling on T_{90} (T_{50}) measurements are explored in this section. We will first investigate the effect of defining postburst background intervals during which there is still burst emission. This is of particular concern in events where there is low-level flux, varying on timescales similar to those of orbital variations in the background rates. We will then address the dependence of T_{90} (T_{50}) on the shape of the background.

Two simulated burst profiles were used to examine the effects of defining the postevent background interval before the end of the event. The burst profiles were FREDs, with a decay time τ_d of 70 s and signal-to-noise ratios S/N of 50 σ and 5.5 σ. The same background model, a fourth degree polynomial, was used for each of the two bursts. The count spectrum used to simulate the burst count rates in each channel is shown in Figure 4.

To characterize how near the postevent background interval is to the burst, we define the parameter

$$x \equiv \frac{t_{b1} - \tau_{95}}{T_{90}}, \tag{29}$$

where t_{b1} is the start time (relative to $t = 0$) of the postevent background interval, and the analytic value of T_{90} given by equation (40) in Appendix B is used. The parameter x measures how much later, in units of T_{90}, the start time of the postburst background interval is than the end time of the T_{90} interval. Low values of x may lead to problems of including source flux in the background fits, and high values of x may not adequately constrain the background model during the time of the burst (particularly, as we will see, when high-order polynomials are used to characterize the background).

We first considered the 50 σ FRED with $\tau_d = 70$ s. By varying t_{b1}, we measured T_{90} and T_{50} for nine different values of x, approximately equally spaced between $\sim$0.0 and 0.8. Though background with a polynomial index of 4 was used during the simulation of the burst, the back-

TABLE 2

SIMULATION RESULTS FOR TIME PROFILES WITH NOISE

TRIANGULAR			RECTANGULAR		FRED		
T_d (s)	T_{90} E_R/E_A (%/σ)	T_{50} E_R/E_A (%/σ)	T_{90} E_R/E_A (%/σ)	T_{50} E_R/E_A (%/σ)	τ_d (s)	T_{90} E_R/E_A (%/σ)	T_{50} E_R/E_A (%/σ)
1.5	<12(45)[a]/1	<12/1	<5/1	<11/1	1.5	<35/1(2)[b]	<20/1(2)[c]
30	<6/1	<2/1	<2/1	<2/1(2)[d]	30	<20/[e]	<10/[e]
150.....	<2/2(4)[f]	<3/2	<1/2	<1/2	70	<20/[e]	<10/[e]

[a] The S/N = 5.5 σ case had $E_R \approx 45\%$, but $E_A < 1\ \sigma$.
[b] The S/N = 10 σ case had $E_A < 2\ \sigma$ and $E_R \approx 35\%$.
[c] The S/N = 15 σ case had $E_A < 2\ \sigma$ and $E_R \approx 15\%$.
[d] The S/N = 30 σ case had $E_A < 2\ \sigma$ and $E_R \approx 1.5\%$.
[e] The measured values are more than 5 σ from analytic value.
[f] The S/N = 10 σ case had $E_A < 4\ \sigma$ and $E_R \approx 2\%$.

© American Astronomical Society • Provided by the NASA Astrophysics Data System

1996ApJ...463..570K

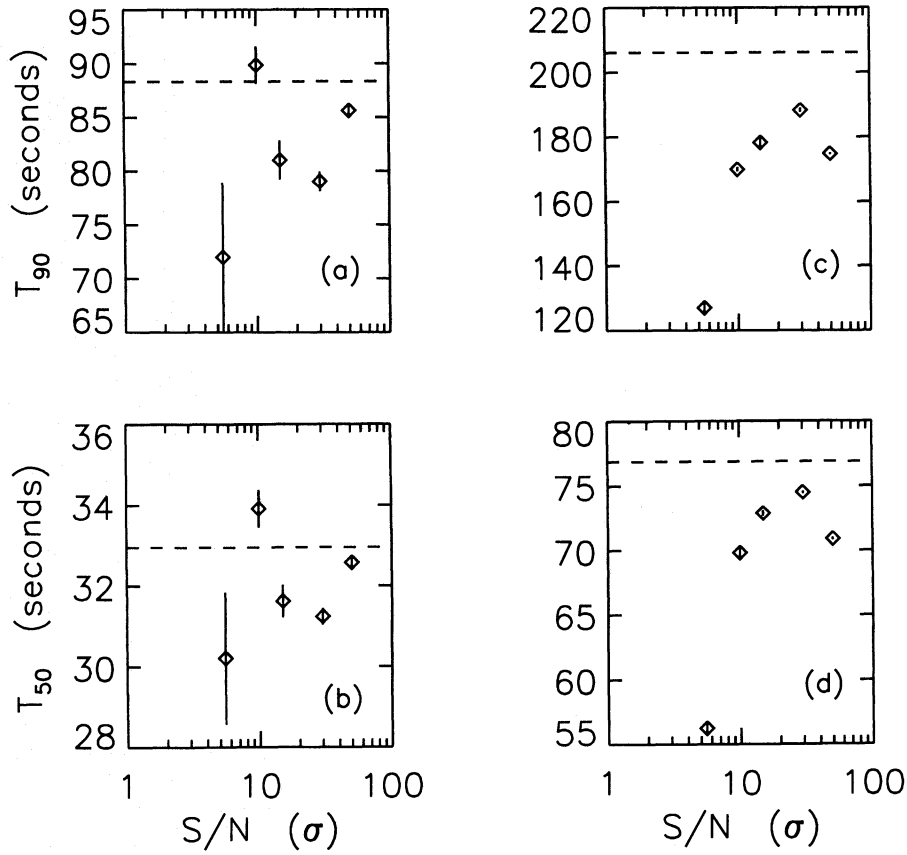

FIG. 7.—(*a*)–(*d*) The measured values of T_{90} and T_{50} as a function of burst S/N for simulated FRED time profiles to which statistical noise has been added. The dashed lines indicate the analytically calculated values of T_{90} and T_{50}. (*a*) and (*c*) as in Fig. 6.

ground was modeled with a polynomial index of 2 during each calculation of T_{90} (it is shown later in this section that low-order polynomials should be used to model background data that are separated by large intervals of source emission). Figures 8*a* and 8*b* show the measured values of T_{90} and T_{50} as a function of x. The measured values are systematically smaller than the analytic values (which are indicated by the dashed lines). The errors in T_{90} and T_{50} were never larger than 30% and 20%, respectively, and in most cases were smaller than these values by a factor of ~ 2. There is also a clear dependence of the measured values of T_{90} and T_{50} on x. The nearer the start of the background intervals to the source emission, the greater the chance of including weak flux in the background model, and the smaller the measured value of T_{90} and T_{50}.

We similarly measured T_{90} (T_{50}) of the 5.5 σ FRED with $\tau_d = 70$ s, using the same nine values of $x(t_{b1})$ as before. A polynomial index of 2 was again used for the background model. The majority of the measured values (Figs. 8*c* and 8*d*) were smaller than the analytic values. The errors in T_{90} and T_{50} were never larger than 33% and 20%, respectively. In spite of larger fluctuations, there is again a clear dependence of T_{90} (T_{50}) on x; T_{90} and T_{50} become smaller the nearer the background interval gets to the event.

To investigate the effects of using a more flexible background model to represent the same background data, we reanalyzed both FREDs, using a polynomial of index 4. The errors are in general worse than for those when the polynomial index of 2 was used. For the 50 σ FRED (see Figs. 9*a* and 9*b*), T_{90} and T_{50} were less than the analytic values by up to 35% and 25%, respectively. The systematic trend for lower values of T_{90} and T_{50} to be derived when lower values of x are used is still apparent. For the 5.5 σ FRED (see Figs. 9*c* and 9*d*), T_{90} and T_{50} were less than the analytic values by up to 55% and 45%, respectively. The systematic dependence of T_{90} and T_{50} on x that is clear in Figures 8, 9*a*, and 9*b* is not seen in Figures 9*c* and 9*d*. This is because at larger values of x, t_{b1} is so near the end of the available data that there is sometimes not enough data in the postburst background interval to adequately constrain high-order polynomial fits. The resulting fits allow too much variation in the interpolated model during the source interval, thus causing improper background subtraction; this effect is clearly more pronounced for weak, long-duration events. We stress that this is caused by the limited amount of simulated data, which ends ~ 360 s after the trigger time. This does in fact mimic the observed data from early in the mission, but during the later part of the mission these data extended out to ~ 550 s, minimizing this effect for all bursts other than those of extremely large duration. Nonetheless, a lower order polynomial (polynomial index of 2 or 3) should be used to fit background data that are separated by large periods of source emission.

We next used simulated bursts to investigate the effects of various background shapes on T_{90} (T_{50}). We randomly selected 10 background models, whose polynomial indices varied between 2 and 4, from those that were used in the BATSE 2B catalog (see discussion of these models at the beginning of § 3.1). We added the same simulated burst to each model. Any discrepancies between the measured and

© American Astronomical Society • Provided by the NASA Astrophysics Data System

1996ApJ...463..570K

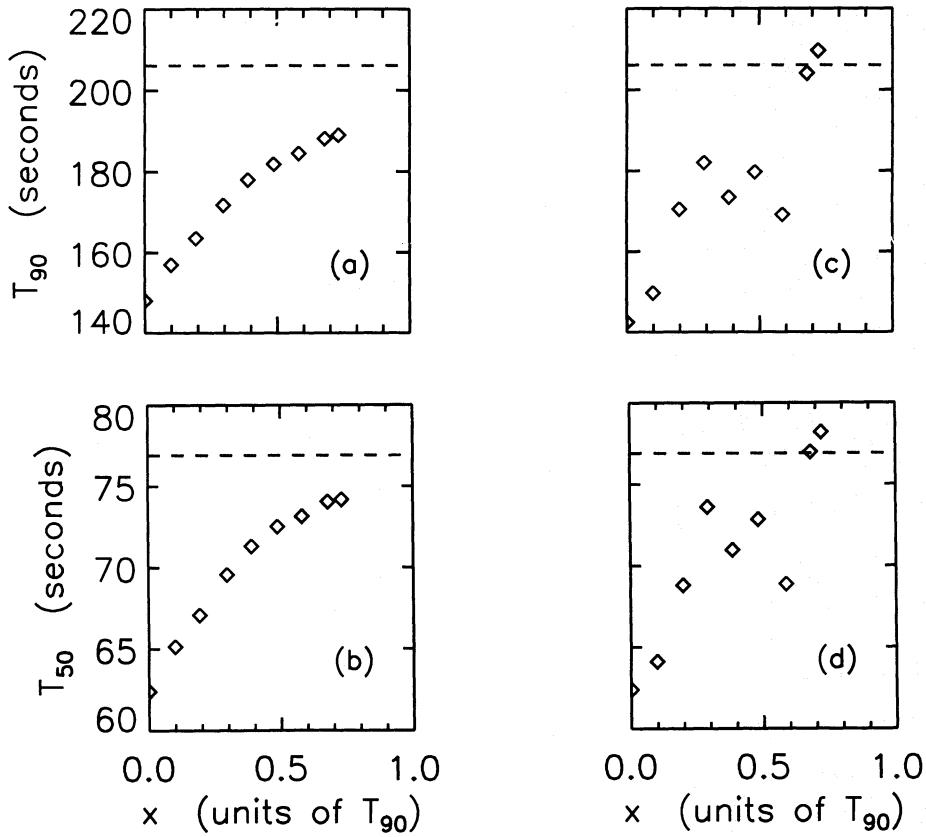

FIG. 8.—(*a*)–(*d*) The measured values of T_{90} and T_{50} as a function of x (defined in the text by eq. [29]) for simulated FRED profiles with $\tau_d = 70$ s. A polynomial of index 4 was used to simulate the background data, but an index of 2 was used to model background during each calculation. The dashed lines indicate the analytically calculated values of T_{90} and T_{50}. (*a*) S/N = 50 σ; (*c*) S/N = 5.5 σ.

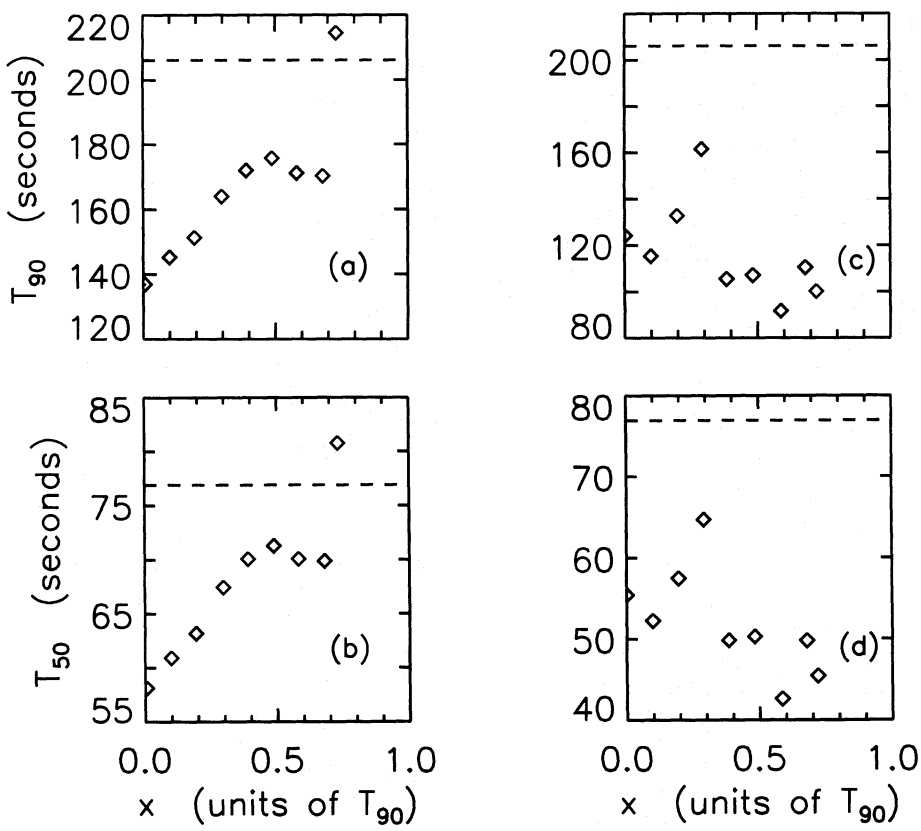

FIG. 9.—(*a*)–(*d*) The measured values of T_{90} and T_{50} as a function of x (defined in the text by eq. [29]) for simulated FRED profiles with $\tau_d = 70$ s. In contrast to the data shown in Fig. 8, a polynomial of index 4 was used to simulate the background data, as well to model background during each calculation. The dashed lines indicate the analytically calculated values of T_{90} and T_{50}. (*a*) and (*c*) as in Fig. 8.

© American Astronomical Society • Provided by the NASA Astrophysics Data System

1996ApJ...463..570K

analytic values would now be a result of the effects of different background shapes (combined, of course, with statistical fluctuations inherent to the measurement process itself). We repeated this procedure with four simulated profiles: a strong and weak triangular burst (both with $T_d = 100$ s), and a strong and weak FRED (both with $\tau_d = 30$ s). The same 10 background models were used for each of the four simulated time profiles. When measuring T_{90} for these simulations, we used polynomials of index 2 to fit the background rates, independent of the index used in the simulation of the rates. This was done to ensure that the background model was sufficiently constrained by the data. As a result, the scatter of the measured values about the analytic values was slightly greater for those profiles which had background rates simulated with a 4th degree polynomial.

Figures 10*a* and 10*b* show the measured values of T_{90} and T_{50}, respectively, for the strong triangular burst with S/N = 50 σ. The *x*-axis values in Figure 10 have no physical meaning, and serve only to identify distinct measurements. The measured values of T_{90} (T_{50}) are scattered about the analytic values (indicated by the dashed lines in Fig. 10), with no tendency for either underestimation or overestimation. The errors in T_{90} and T_{50} were less than 1%. The errors (see Figs. 10*c* and 10*d*) associated with the weaker triangular burst, with S/N = 5.5 σ, were less than 8%. The scatter of the measured values about the analytic values is larger for the weaker burst, but we do not find any tendency for either underestimation or overestimation.

The errors in T_{90} and T_{50} (see Figs. 11*a* and 11*b*) for the strong FRED, with S/N = 50 σ, were less than 4%, except for one measurement of T_{90} which had an error of $\sim 10\%$. There is a slight trend for the measured values to be underestimated; however, this can be attributed to the previously discussed effects of large values of *x*, and not to the varying background shapes. The errors in T_{90} and T_{50} (Figs. 11*c* and 11*d*) for the weaker FRED, with S/N = 5.5 σ, were less than 30% and 20%, respectively. Again, the scatter of the measured values about the analytic values is larger for the weaker burst. We thus find no significant dependence of the measured values of T_{90} (T_{50}) on the shape of the background.

3.2. *Reduction of the Signal-to-Noise Ratio of Observed Gamma-Ray Burst Profiles*

To gain insight into the systematic effects associated with the detailed burst profile shapes, we chose several bursts observed with BATSE, systematically reduce their intensity, and in each case measure their T_{90} and T_{50}. We will first describe the details of the signal-to-noise reduction of the observed bursts; our results will be discussed in § 3.2.1.

The time histories of each observed burst consist of LAD count rates $\Delta C(E, t)/\Delta t$ in the four BATSE discriminator energy channels, with a time resolution as described in § 2.2. Background data before and after the burst are fitted to a polynomial function of order between 2 and 4, and the background model $\Delta B(E, t)/\Delta t$ is created by interpolating the fit across the burst interval. Each energy channel is modeled independently. This background model is saved and is used for all reductions of the S/N of this burst.

The source count rates $\Delta S(E, t)/\Delta t$ are found by subtracting the background model rates from the observed count

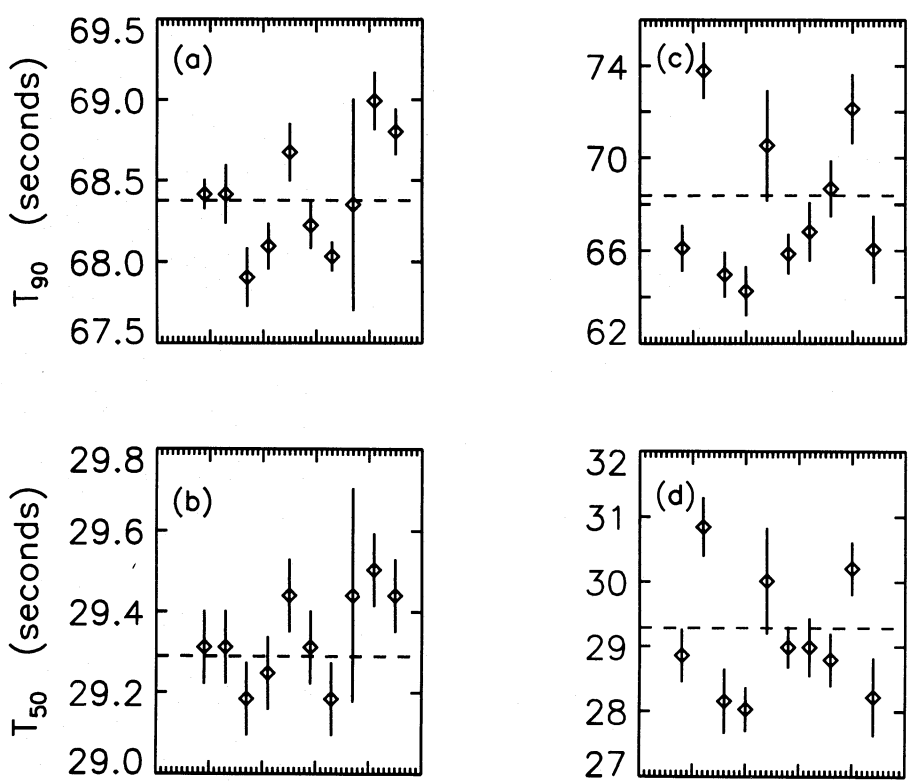

FIG. 10.—(*a*)–(*d*) The measured values of T_{90} and T_{50} for two different simulated triangular profiles, both with a duration $T_d = 100$ s, using the same set of 10 background models for each simulation. The *x*-axis has no physical meaning and only serves to distinguish between different simulations. The dashed lines indicate the analytically calculated values of T_{90} and T_{50}. (*a*) and (*c*) as in Fig. 8.

© American Astronomical Society • Provided by the NASA Astrophysics Data System

1996ApJ...463..570K

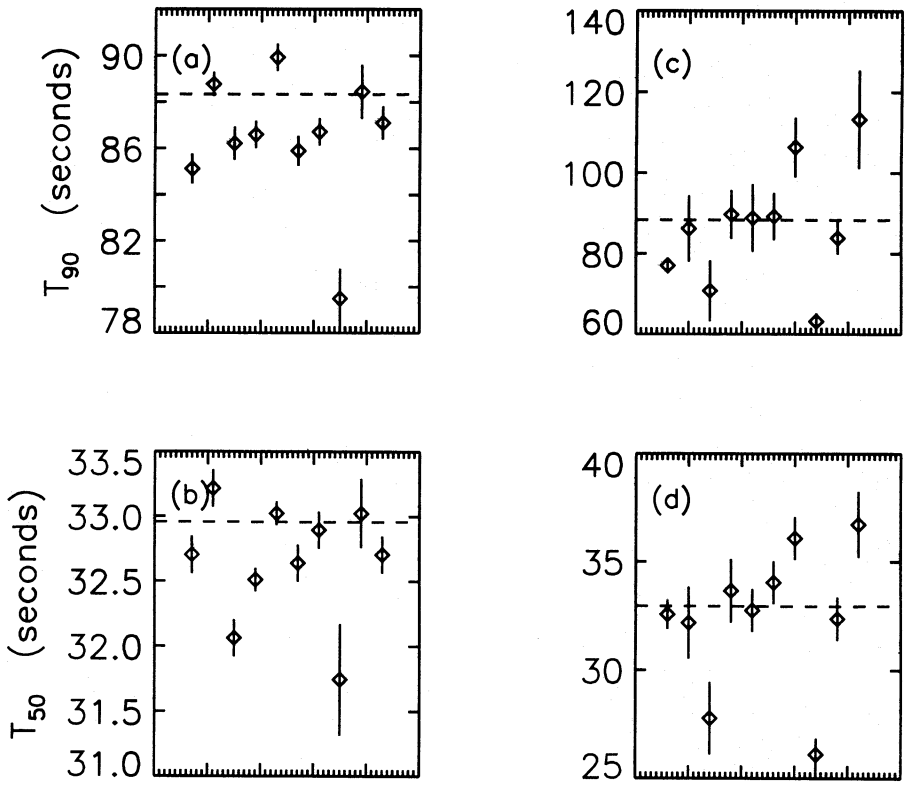

FIG. 11.—(*a*)–(*d*) The measured values of T_{90} and T_{50} for two different simulated FRED profiles, both with $\tau_d = 30$ s, using the same set of 10 background models for each simulation. The *x*-axis has no physical meaning and only serves to distinguish between different simulations. The dashed lines indicate the analytically calculated values of T_{90} and T_{50}. (*a*) and (*c*) as in Fig. 8.

rates in each channel,

$$\frac{\Delta S(E, t)}{\Delta t} = \frac{\Delta C(E, t)}{\Delta t} - \frac{\Delta B(E, t)}{\Delta t} . \tag{30}$$

The counts $\Delta C(E_i, t_j)$, $\Delta S(E_i, t_j)$, and $\Delta B(E_i, t_j)$ in each time bin are calculated.

We use the count rates $\Delta S(E, t)/\Delta t$ as a template for the source rates, thus making the assumption that these rates are free of any statistical fluctuations. Note that we use the same template to create the time histories over the entire range of intensities, otherwise we would magnify the statistical fluctuations that are inherent to $\Delta C(E, t)/\Delta t$.

The time $t_{\rm pk}$ of the peak count rate was determined using the data summed over energy channels 2 and 3. Assuming that the background counts are Poissonian, the statistical noise $\sigma_{\rm pk}$ at the peak time is given by

$$\sigma_{\rm pk} = \sqrt{\Delta B_{\rm pk}} , \tag{31}$$

where $\Delta B_{\rm pk}$ is the number of background counts observed during the data interval containing the peak rate. The signal-to-noise ratio of the peak, $({\rm S/N})_{\rm pk}$, is then given by

$$({\rm S/N})_{\rm pk} = \frac{\Delta S_{\rm pk}}{\sigma_{\rm pk}} , \tag{32}$$

where $\Delta S_{\rm pk}$ is the number of counts observed above background during the data interval containing the peak rate.

The signal-to-noise to which the burst is to be reduced is designated as $({\rm S/N})_r$. The reduced source counts $\Delta S_r(E, t)$ are then found from

$$\Delta S_r(E_i, t_j) = \zeta \Delta S(E_i, t_j) , \tag{33}$$

where ζ is defined as

$$\zeta \equiv \frac{({\rm S/N})_r}{({\rm S/N})_{\rm pk}} . \tag{34}$$

Note that this process involves reducing the source counts in each bin by the same multiplicative factor, and does not involve subtracting a constant from each bin. Thus the ratio between the source counts in any two time bins will remain constant.

The reduced total count rates $\Delta C_r(E, t)/\Delta t$ are produced using the same method described in § 3.1 (see eqs. [26] through [28]). The reduced source rates are first combined with the background model, then an appropriate level of statistical noise is added. After each simulation we confirmed that BATSE would have triggered at some time on at least one of the three timescales.

3.2.1. *Dependence of T_{90} on Signal-to-Noise Ratio for Various Time Profile Shapes*

We applied the procedure described in § 3.2 to a group of 12 GRBs, (shown in Figs. 12 and 13, summed over channels 1 through 4) observed with BATSE. We tried to include a variety of profile shapes in this group. The values of T_{90} (T_{50}) cannot be calculated analytically for these observed bursts. Instead of quoting the relative errors and absolute errors as in § 3.1.1 and 3.1.2, we will examine relative and absolute differences (D_R and D_A), with respect to the values measured for the originally observed unreduced burst. Table 3 lists the values of peak S/N to which each burst was reduced, as well as the maximum values of D_R and D_A for both T_{90} and T_{50}.

© American Astronomical Society • Provided by the NASA Astrophysics Data System

1996ApJ...463..570K

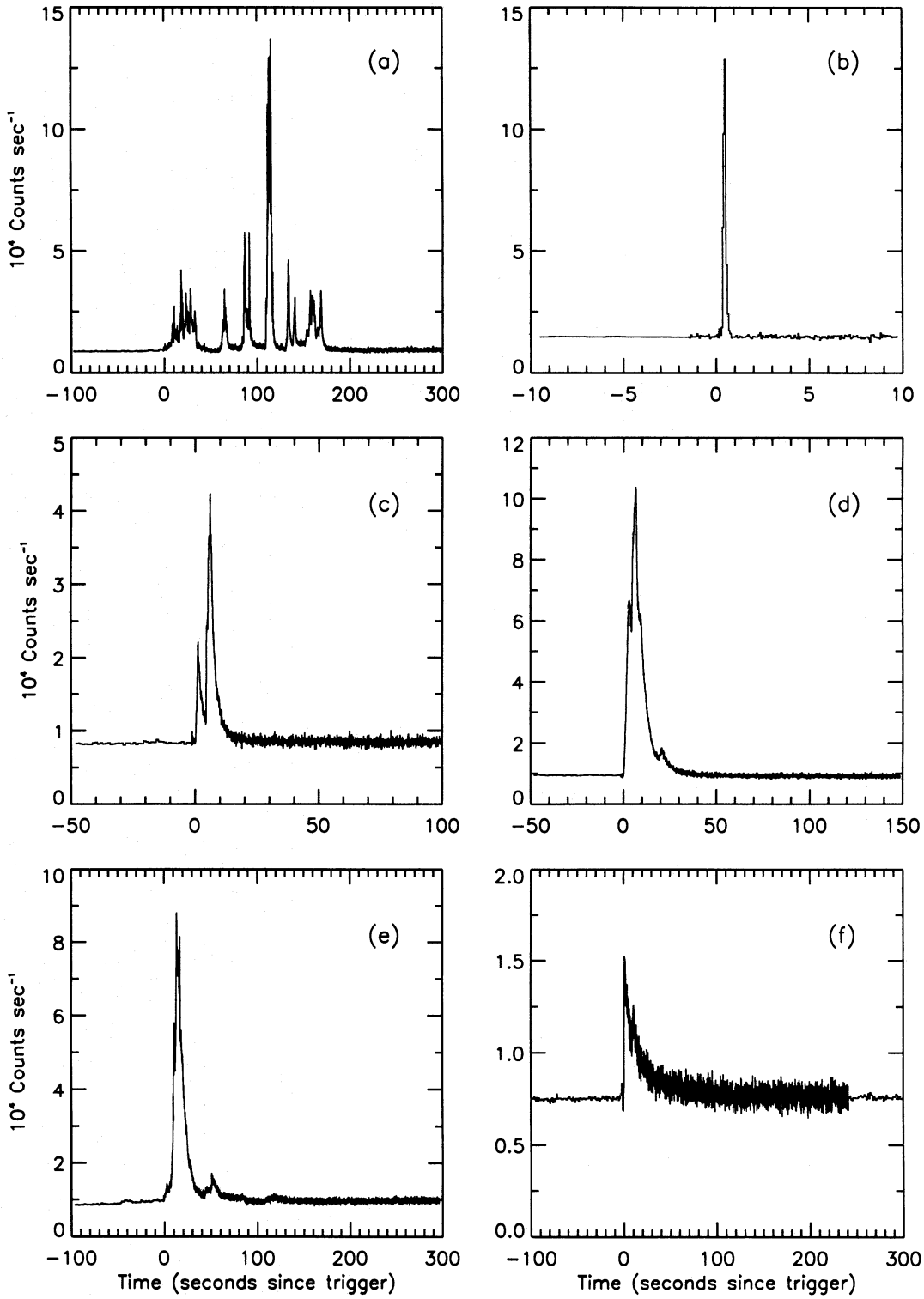

FIG. 12.—Time profiles of six gamma-ray bursts observed with BATSE that were chosen to investigate the dependence of T_{90} and T_{50} on various observed profile shapes. (*a*) Burst 3B 940217. (*b*) Burst 1B 910626. (*c*) Burst 1B 910627. (*d*) Burst 1B 911118. (*e*) Burst 3B 940206. (*f*) Burst 1B 910602.

The first burst examined, 3B 940217 (Fig. 12*a*) has a long, complex time profile, with some weak emission near the beginning and end of the event. Figure 14 shows each of the reduced time profiles of 3B 940217, except for the case of S/N = 200 σ. Figures 15*a* and 15*b* show the measured values of T_{90} and T_{50} as a function of the reduced burst S/N. The dashed lines indicate the unreduced values of T_{90} and T_{50}. The measured values of T_{90} and T_{50} for the S/N = 5.5 σ case are underestimated; however, we find no systematic trend in the measured values as a function of the burst S/N. Note that the size of the statistical uncertainties δT_{90} and δT_{50} are inversely proportional to the burst S/N. This was true for each of the 12 bursts examined.

The profile of the second burst, 1B 910626 (Fig. 12*b*),

© American Astronomical Society • Provided by the NASA Astrophysics Data System

1996ApJ...463..570K

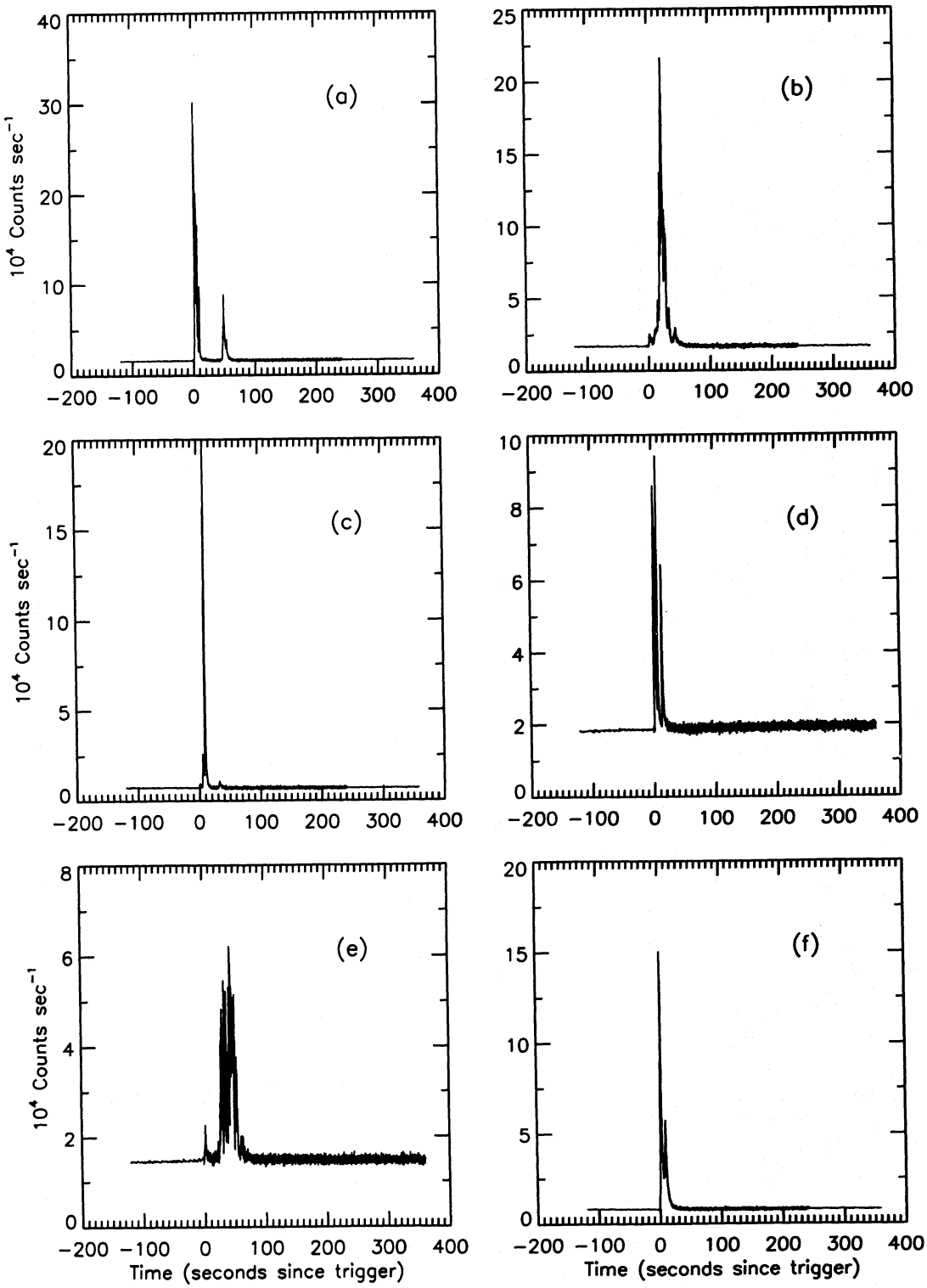

FIG. 13.—Time profiles of six gamma-ray bursts observed with BATSE that were chosen to investigate the dependence of T_{90} and T_{50} on various observed profile shapes. (*a*) Burst 1B 910503. (*b*) Burst 1B 910601. (*c*) Burst 1B 920517. (*d*) Burst 1B 940429. (*e*) Burst 3B 940817. (*f*) Burst 1B 921207.

consisted of a short single pulse. We find no systematic dependence of the measured values of T_{90} or T_{50} on the burst S/N. In fact, the measured values of T_{90} and T_{50} for the reduced bursts were the same as the unreduced value except for the case of S/N = 5.5 σ, where the difference in T_{90} and T_{50} were $\sim$140% and $\sim$50%, respectively (both still within 1 σ). These large relative differences were due to the fact that for short duration bursts, with extremely low values of S/N, the total counts observed from fluctuations in background is comparable to the total counts observed from the burst itself. Thus it is difficult to accurately determine the zero-fluence and total-fluence levels.

Burst 3B 940206 (Fig. 12e) shows a pulse with substructure, surrounded by weak extended emission on both sides.

© American Astronomical Society • Provided by the NASA Astrophysics Data System

1996ApJ...463..570K

TABLE 3

RESULTS OF S/N REDUCTION OF OBSERVED BURSTS

Burst Name	S/N (σ)	T_{90} D_R/D_A (%/σ)	T_{50} D_R/D_A (%/σ)
3B 940217.....	350,[a] 200, 100, 50, 30, 15, 5.5	<4/3	<3(30)[b]/2[c]
1B 910626.....	240,[a] 100, 50, 15, 5.5	<1(140)[d]/1	<1(50)[e]/1
1B 910627.....	84,[a] 50, 30, 15, 5.5	<40(70)[f]/2(4)[g]	<10/2
1B 911118.....	270,[a] 200, 100, 50, 15, 5.5	<3/1	<3/1
3B 940206.....	210,[a] 100, 50, 30, 15, 5.5	<38/[c]	<25/[c]
1B 910602.....	21,[a] 15, 10, 5.5	<4/1	<4(9)[h]/1
1B 910503.....	590,[a] 500, 300, 200, 100, 50, 30, 15, 5.5	<3/1	<3(280)[i]/1/(3)[i]
1B 910601.....	406,[a] 200, 100, 50, 30, 15, 5.5	<7/2	<3(10)[j]/2
3B 920517.....	583,[a] 400, 200, 100, 50, 30, 15, 5.5	<60/3	<25/2
3B 940429.....	150,[a] 100, 50, 30, 15, 5.5	<17/1	<3/1
3B 940817.....	106,[a] 50, 30, 15, 5.5	<15(40)[k]/3	<10/2
3B 921207.....	438,[a] 200, 100, 50, 30, 15, 5.5	<14(22)[l]/2	<5/1

[a] This is the S/N of the unreduced observed gamma-ray burst.
[b] The S/N = 5.5 σ case had $D_A > 5\,\sigma$ and $D_R \approx 30\%$.
[c] The measured values are more than 5 σ from the unreduced value.
[d] The S/N = 5.5 σ case had $D_R \approx 140\%$ and $D_A < 1\,\sigma$.
[e] The S/N = 5.5 σ case had $D_R \approx 50\%$ and $D_A < 1\,\sigma$.
[f] The S/N = 30 σ case had $D_R \approx 70\%$ and $D_A < 2\,\sigma$.
[g] The S/N = 30 σ case had $D_A < 4\,\sigma$ and $D_R \approx 40\%$.
[h] The S/N = 10 σ case had $D_R \approx 9\%$ and $D_A < 1\,\sigma$.
[i] The S/N = 15 σ case had $D_R \approx 280\%$ and $D_A < 3\,\sigma$.
[j] The S/N = 5.5 σ case had $D_R \approx 10\%$ and $D_A < 1\,\sigma$.
[k] The S/N = 5.5 σ case had $D_R \approx 40\%$ and $D_A < 3\,\sigma$.
[l] The S/N = 5.5 σ case had $D_R \approx 22\%$ and $D_A < 1\,\sigma$.

The differences in T_{90} and T_{50} (see Figs. 15*c* and 15*d*) are all less than 38% and 25%, respectively. All of the measured values became systematically smaller as the burst S/N was decreased, similar to the behavior exhibited by the simulated FREDs in § 3.1.2.

Burst 3B 920517 (Fig. 13*c*) contains a weak pulse at the trigger time, followed ~4 s later by a strong multipeaked pulse of ~10 s duration, and then a substantially weaker pulse ~15 s later. Though the measured values were not systematically larger or smaller as a function of burst S/N, we did find that the differences in T_{90} were approximately 45% for both the 100 σ and 50 σ cases. The measured values of T_{50} for these two cases, however, were identical to that measured for the original unreduced burst. Large deviations at such high values of S/N were not common. Excluding bursts 3B 920517 and 3B 940206, and the 30 σ case of burst 1B 910627, the relative differences for bursts with S/N > 15 σ were less than 7% and 5% for T_{90} and T_{50}, respectively

The remaining bursts showed no systematic dependence on the burst S/N, other than an increase in the scatter of the measured values about the unreduced values.

4. T_{90} AND T_{50} DISTRIBUTIONS

Though the measured values of T_{90} (T_{50}) for an event observed simultaneously with two different instruments may be consistent, the distributions of these parameters observed by each instrument may be quite different. This can be attributed to different (though likely overlapping) populations of burst sources being sampled.

A distinction must be made between four possible T_{90} distributions. The first, and most fundamental, is the *parent* distributions of the *intrinsic* T_{90} s. This is the distribution that would be measured by a set of perfect (free of statistical noise and background, and having a Detector Response Matrix equal to the Identity matrix) bolometric detectors, with one detector located in an inertial frame of each burst source in the universe. These T_{90} s directly result from the burst emission mechanisms. If burst sources are at distances of ~1 Gpc, where cosmological effects become important, then this distribution may evolve as a function of cosmic look-back time.

The second distribution is the *parent* distribution of *extrinsic* T_{90} s, and consists of one extrinsic T_{90} for every burst that occurs in the universe. These T_{90} s are extrinsic in that they are a convolution of the true distribution of intrinsic T_{90} s with the effects of *propagation* of the radiation from the source to the detector. These propagation effects would include time dilation and redshift effects resulting from cosmological expansion of the universe and any interaction of the burst radiation with intervening matter or the background radiation. The parent distribution of extrinsic T_{90} s would be measured by a perfect bolometric detector, located in the current epoch, that detects every burst that occurs in the universe.

The third distribution is the *selected* distribution of *extrinsic* T_{90} s. It is a convolution of the parent distribution of extrinsic T_{90} s with the detection criteria and instrumental response of the observing detector. The BATSE observation of this distribution is shown in Figure 16*a*; this distribution will be different for different instruments.

The fourth distribution is the *selected* distribution of *intrinsic* T_{90} s. This distribution is obtained by deconvolving the propagation effects (but not the detection selection criteria) from the selected distribution of extrinsic T_{90} s. This is the most fundamental distribution that can be hoped to be obtained from the observational data. To obtain the parent distribution of intrinsic T_{90} s would require full knowledge of the parent distribution of extrinsic T_{90} s, which is forbidden by the detection criteria of our imperfect detectors. At best, the fourth distribution may place constraints on the parent distribution of intrinsic T_{90} s.

© American Astronomical Society • Provided by the NASA Astrophysics Data System

1996ApJ...463..570K

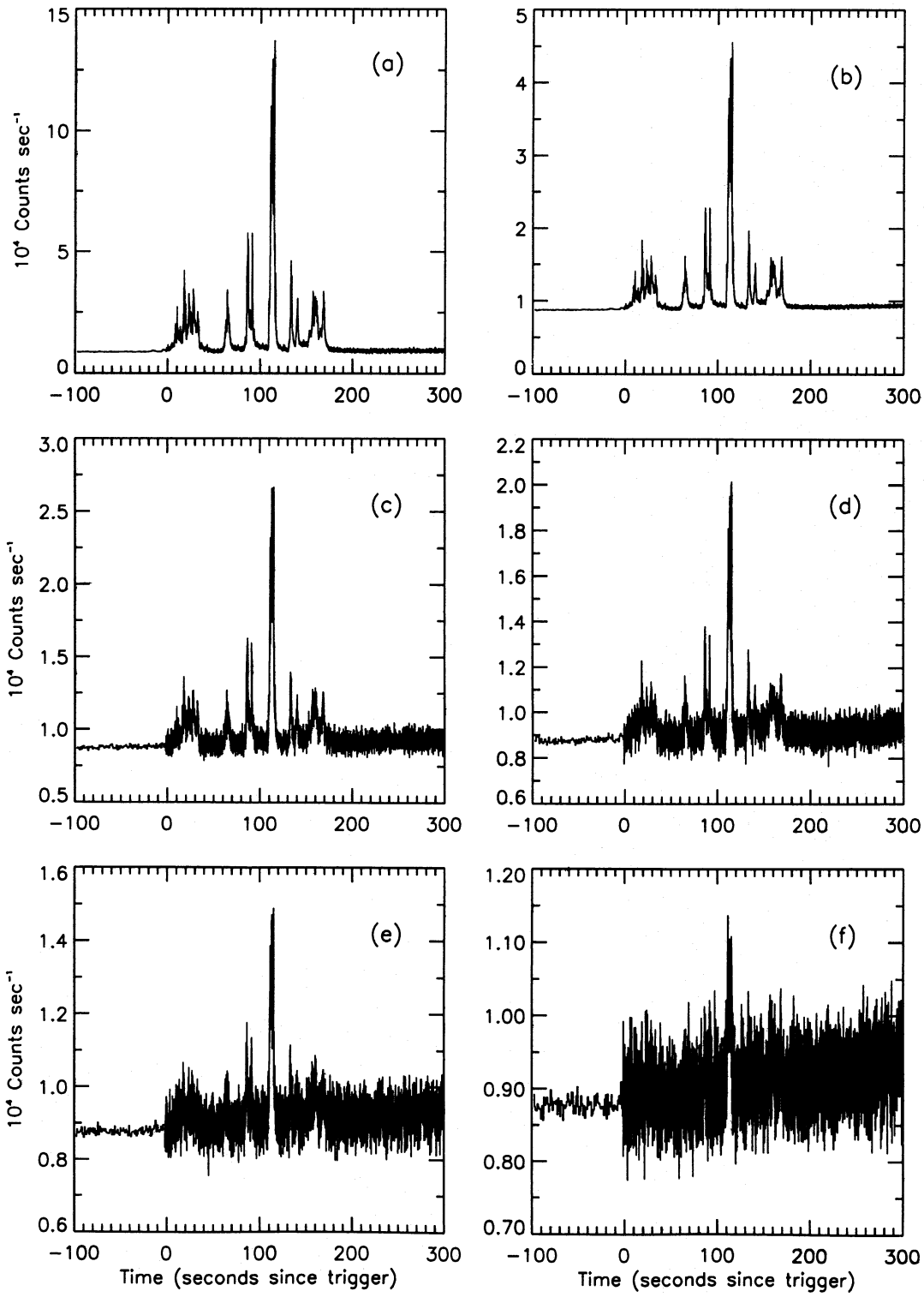

FIG. 14.—Time profiles of burst 3B 940217 with various peak S/N ratios. (*a*) Observed S/N = 350 σ. (*b*) Reduced S/N = 100 σ. (*c*) Reduced S/N = 50 σ. (*d*) Reduced S/N = 30 σ. (*e*) Reduced S/N = 15 σ. (*f*) Reduced S/N = 5.5 σ.

There are a number of factors that contribute to the shape of the selected distribution of extrinsic T_{90} s, resulting in different sampling regions of the parent distribution of extrinsic T_{90} s for two different instruments. One important factor would be a difference in on board trigger criteria. For instance, different trigger timescales sample different distance ranges. The magnitude of this effect depends on both the duration of the burst and on the shape of the time profile during the trigger time interval. The shorter trigger timescales sample short bursts out to further distances than the longer trigger timescales, and the longer trigger timescales sample longer bursts out to further distances. Thus, if possible, T_{90} (T_{50}) distributions should be examined independently for each trigger timescale, with each distribution containing only those bursts that would have triggered that timescale at some time. The distributions for all trigger

© American Astronomical Society • Provided by the NASA Astrophysics Data System

1996ApJ...463..570K

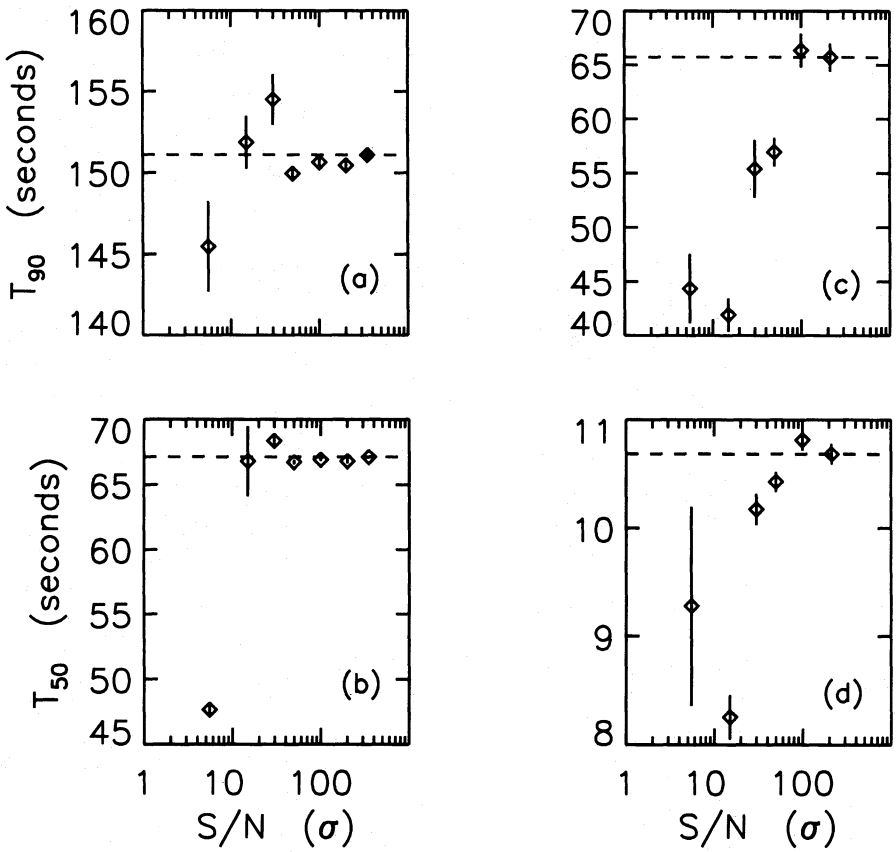

FIG. 15.—(*a*)–(*d*) The measured values of T_{90} and T_{50} for two of the profiles which have had their S/N reduced. The dashed lines indicate the values of T_{90} and T_{50} as measured for the originally observed (unreduced) bursts. (*a*) Burst 3B 940217. (*c*) Burst 3B 940206.

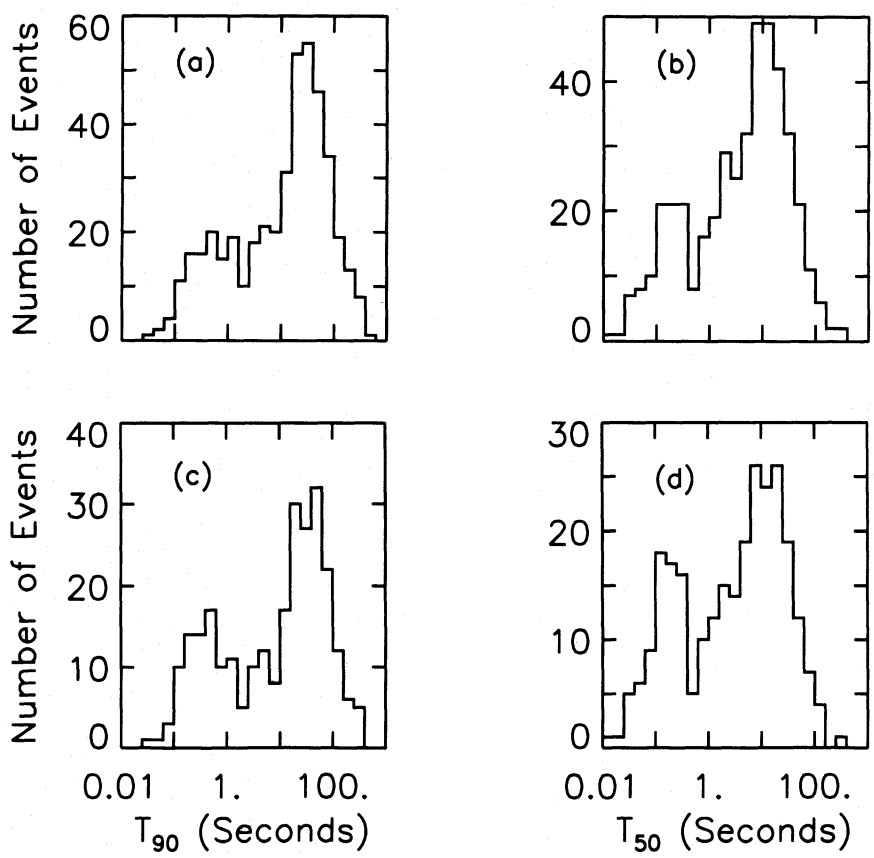

FIG. 16.—(*a*)–(*b*) The observed distributions of T_{90} and T_{50} as measured for the BATSE 2B Catalog. (*c*)–(*d*) The observed distributions of T_{90} and T_{50} for those 267 bursts in the BATSE 2B catalog that would have triggered on the BATSE 64 ms trigger timescale.

© American Astronomical Society • Provided by the NASA Astrophysics Data System

1996ApJ...463..570K

timescales cannot be combined without detailed knowledge of the distribution of profile shapes during the trigger time interval

One should not make the mistake of thinking that bursts with durations less than t_{trg} that have low values of peak intensity are missing from the selected distributions. This is because the term "peak intensity" is meaningless unless the timescale on which it is measured is also specified. Rather, the selected distributions of T_{90} (T_{50}) are flux-complete on each individual trigger timescale. Instrument trigger criteria require the accumulation of a minimum number of counts $(C_{min})_{t_{trg}}$ on a specific trigger timescale t_{trg} in a specified energy range. All events that result in at least this minimum number of counts observed during the trigger time interval will trigger the instrument. Thus the T_{90} (T_{50}) distributions are complete down to a flux of $(C_{min})_{t_{trg}}$ counts in t_{trg} s. This completeness will, of course, shape the short end of the selected distributions of extrinsic T_{90} s (T_{50} s). The number of counts $(C_{min})_{t_{trg}}$ is calculated based on an assumed number of background counts expected during the trigger time interval. If the burst duration is less than t_{trg}, then this assumed background level will be an overestimate on the timescale of the duration of the burst. On this timescale, the intensity will need to be higher than the threshold intensity as measured on the longer timescale t_{trg}. Thus the region of the parent distribution of extrinsic T_{90} s with durations less than t_{trg} will not be completely sampled by any real detector, only the population of these bursts with $(C_{min})_{t_{trg}}$ counts on the trigger timescale t_{trg} will be included in the selected distribution of extrinsic T_{90} s.

We stress that this completeness effect should not be misinterpreted as triggering on fluence. The instrument trigger criteria are not a function of burst duration; it always triggers on the number of counts detected above background during a trigger time interval. For those bursts with durations less than t_{trg}, all source counts (i.e., the burst fluence) may be observed within the trigger interval.

The trigger threshold of an instrument will also significantly affect the selected distributions of extrinsic T_{90} s. The threshold is partly a function of the local background environment. For example, the observed local background of a detector flown in a near-Earth orbit is quite different from that of an interplanetary probe. The threshold is also dependent on the collecting area of the detector as well as the onboard software triggering criteria. An instrument with a lower threshold will observe a sample of less luminous bursts that would not trigger a detector of higher threshold. In addition, the instrument with a higher threshold will sample a smaller region of the short-end of the parent distribution of extrinsic T_{90} s because of the flux-completeness of the selected sample.

Another trigger criterion often different between various detectors is the trigger energy range. Because of the diversity of the photon spectra of GRBs, triggers examining different regions of the spectrum will select different samples of events (of course with some overlap).

4.1. *Measurements Made with BATSE*

The selected distributions of 433 extrinsic T_{90} s and T_{50} s, as measured for the set of GRBs in the BATSE 2B catalog (Meegan et al. 1994), are shown in Figures 16*a* and 16*b*. Kouveliotou et al. (1993) reported that the distributions are bimodal, with a short group ($T_{90} < 2$ s) and a long group ($T_{90} > 2$ s). This result is consistent with previous measurements of the observed GRB duration distributions (Hurley, 1992 and references therein). However, the explanation behind this bimodality remains unknown. The deficiency of bursts is in the region $T_{90} \approx 2$ s, which is a factor of ~ 2 larger than the largest BATSE trigger timescale of 1.024 s. The turnover in the T_{90} distribution at values lower than 1 s, at least in part, reflects the above discussed effect of flux-completeness of the selected distributions.The turnover at large values of T_{90} is most likely real, though the largest observed value is probably a result of the finite sampling of the parent distribution.

We have performed a nonlinear least-squares fit to the observed T_{90} distribution using a function that represents the sum of two log-normal Gaussians, given by

$$f(T_{90}) = \frac{A_s}{\sigma_s} \exp\left[-\left(\frac{\log T_{90} - \log \mu_s}{\sigma_s}\right)^2\right] + \frac{A_L}{\sigma_L} \exp\left[-\left(\frac{\log T_{90} - \log \mu_L}{\sigma_L}\right)^2\right]. \quad (35)$$

We find that the best-fit values are $\mu_s = 0.60 \pm 0.11$ s, $\sigma_a = 1.21 \pm 0.14$, and $\mu_L = 32.1 \pm 2.6$ s, $\sigma_L = 1.06 \pm 0.07$. The reduced χ^2 of the fit is 0.816 for 15 degrees of freedom ν ($\nu = 15$), giving $P(\chi^2, \nu) = 0.66$.

If one examines only the bursts that would have triggered the 64 ms trigger timescale, the bimodality becomes more distinct. Figures 16*c* and 16*d* show the T_{90} and T_{50} distributions for those 267 BATSE bursts that would have triggered on at least the 64 ms trigger timescale. For this sample we find $\mu_s = 0.47 \pm 0.07$ s, $\sigma_s = 1.06 \pm 0.12$, and $\mu_L = 34.9 \pm 3.2$ s, $\sigma_L = 1.01 \pm 0.08$. The reduced χ^2 of the fit is 0.964 for 14 degrees of freedom ν ($\nu = 14$), giving $P(\chi^2, \nu) = 0.49$. Thus the effect of limiting the sample to the smallest trigger timescale is to shift the centroid of the short population to a lower value of T_{90} and to shift that of the long population to a higher value. However, the best-fit values for the single timescale sample are within 1 σ of the sample containing bursts that triggered on any of the three timescales.

The distributions shown in Figures 16*c* and 16*d* are slightly flux-biased. This is because once the BATSE onboard burst trigger is set, the 256 and 1024 ms trigger timescales are disabled, and the trigger threshold of the 64 ms trigger timescale is adjusted such that only an event stronger than the already triggered burst can retrigger the instrument. The three trigger thresholds are reset to their nominal values after the readout of burst data from the triggered burst is completed. Thus, bursts which occur during the readout of data from a previous burst, have a peak flux larger than nominal 5.5 σ above background on the 64 ms timescale, but are weaker than the previous burst on this timescale, will not be included in the sample.

One can examine the region of the selected distributions that is nearly free of the effects of flux-completeness, by limiting the data to values of T_{90} greater than the shortest trigger timescale. Fitting only data with $T_{90} > 0.1$ s to the model given in equation (35), we find that the best-fit parameters are given by $\mu_s = 0.56 \pm 0.17$ s, $\sigma_s = 1.68 \pm 0.57$, $\mu_L = 34.3 \pm 3.7$ s, and $\sigma_L = 1.02 \pm 0.08$. The reduced χ^2 of the fit is 0.84 for 12 degrees of freedom ν ($\nu = 12$), giving $P(\chi^2, \nu) = 0.61$. Again, the best-fit values for this limited sample are within 1 σ of the unlimited sample.

If GRB sources are at distances of several Gpc, then the temporal properties of their emitted radiation should

© American Astronomical Society • Provided by the NASA Astrophysics Data System

1996ApJ...463..570K

exhibit the effects of time dilation (Weinberg 1972). $(T_{90})_o$, the value of T_{90} for a burst at a cosmological redshift of z as observed by a detector at the present epoch, is related to $(T_{90})_i$, the intrinsic value of T_{90} that would be observed by a detector in a comoving frame near the source, through the relation $(T_{90})_o = (1 + z)(T_{90})_i$. Thus, one may predict that weak bursts, which are *on average* further away, should *on average* have larger values of $(T_{90})_o$. The same effect would be expected from an anticorrelation between the peak luminosity of a burst and its duration (which would be, for example, required if the total energy associated with each burst is constant). We have shown that in most cases T_{90} (T_{50}) is not subject to systematic effects that are a function of S/N; the exception (primarily due to inadequate background modeling) being the case of bursts with weak extended emission. These types of profiles show a tendency for the values of T_{90} (T_{50}) to be systematically *underestimated* for low values of S/N. Notice that this works to weaken the signatures of cosmological time dilation or of a luminosity-duration anticorrelation if either is present in the BATSE T_{90} (T_{50}) distributions, but perhaps more importantly, would not introduce either of them.

4.2. *Measurements Made with Other Instruments*

Kargatis et al. (1994) determined T_{50} for 171 GRBs observed with the SIGNE experiments on board the *Venera 13* and *14* satellites. SIGNE had a smaller detector area than a BATSE LAD, required an 8 σ fluctuation on a 1.024 s timescale to trigger, and had a memory size that allowed data collection for 62 s. The extrinsic T_{50} distribution observed with SIGNE shows a single peak at ~ 6 s, with a cutoff at $T_{50} > 64$ s due to the limited memory size, and a decaying tail extending from the peak down to small values of T_{50}. Below the 64 s cutoff, this peak is consistent with the high peak observed in the BATSE T_{50} distribution. The SIGNE distribution does not show the second peak at small values of T_{50} that is observed in the BATSE distribution (Kouveliotou et al. 1993). Kargatis et al. (1994) report that the fraction of SIGNE bursts with $T_{50} < 0.6$ s is 15%, as compared to 25% for the BATSE 1B catalog. Though these numbers are correct, they should have compared the SIGNE sample of bursts with those bursts observed with BATSE that would have triggered only the 1.024 s trigger timescale. In this case, the fraction of BATSE bursts with $T_{50} < 0.6$ s is $\sim 15\%$ for both the BATSE 1B and 2B catalogs.

Terekhov et al. (1994, 1995) determined the extrinsic T_{90} for 118 GRBs observed with the PHEBUS instrument on board the *GRANAT* satelite. PHEBUS consisted of six bismuth germanate (BGO) scintillation detectors, one on each side of the spacecraft. The maximum effective geometrical area is ~ 420 cm^2, ~ 5 times smaller than that of a BATSE LAD. PHEBUS required an 8 σ fluctuation above background on either a 0.25 or 1.024 s timescale to trigger. PHEBUS also triggers in a higher energy range (0.1–1 MeV) than BATSE (50–300 keV), thus PHEBUS will selectively choose a sample of bursts from the true distribution of observed T_{90} s with harder spectra than those selected with BATSE.

The extrinsix T_{90} distribution observed with PHEBUS consisted of a single pulse peaking at ~ 10–20 s, with an upper cutoff at $T_{90} \approx 200$ s, and a decaying tail extending from the peak down to smaller values of T_{90}. The PHEBUS distribution does not show a second peak at small values of T_{90}. Nevertheless, Terekhov et al. (1994, 1995) report that the fraction of PHEBUS bursts with $T_{90} < 2$ s is 23%, consistent with that reported by BATSE. This lack of a second peak in the PHEBUS sample of 118 events may simply be due to the better statistics afforded by the larger BATSE sample. It may also be due in part to the differing selection criteria of the two instruments. Convolving the differing trigger energy ranges with the observation that bursts with $T_{90} > 2$ s show softer spectra in the BATSE data than those events with $T_{90} < 2$ s (Dezalay et al. 1992; Kouveliotou et al. 1993) may lead to a deficiency of weak events in the PHEBUS data set with $T_{90} > 2$ s. In addition, the flux-completeness caused by the lack of a 64 ms trigger timescale on PHEBUS necessitates that PHEBUS samples a different set of bursts at the shortend of the extrinsic duration distribution than does BATSE.

5. SUMMARY

We have provided an extensive description of how T_{90} (T_{50}), and their statistical uncertainties, are measured for GRBs observed with BATSE. Using simulated simple noiseless time profiles, we were able to show that the standard software used by the BATSE team to calculate T_{90} (T_{50}) is working properly. The only noticeable error, which is unavoidable, is that due to the finite binning inherent to the data. We also find that in the noise-free cases with slowly varying source flux, it can be difficult to distinguish source flux from background variations, result in errors in T_{90} up to $\approx 20\%$ (see the case of the FRED profiles with τ_d of 70 s).

We have investigated the systematic effects associated with the measurement of T_{90} and T_{50} for simulated bursts, to which statistical noise was added. Three profile shapes were simulated for a number of combinations of S/N and duration. The values of T_{90} (T_{50}) measured for the rectangular and triangular profiles agreed fairly well with the values calculated analytically; we found no evidence for any systematic dependence of either T_{90} or T_{50} on the burst S/N. Statistical fluctuations in background can have fluences comparable to the fluence of short bursts, and become a limiting factor in the accuracy of T_{90} (T_{50}). As in the noise-free simulations, the largest errors in the measured values of T_{90} (T_{50}) were observed with the case of FRED profiles. We found that the measured values of T_{90} (T_{50}) were on average *underestimated* by $\leq 20\%$ (10%) for the two FRED profiles with τ_d of 30 and 70 s. In addition, we found a systematic dependence of T_{90} (T_{50}) on the burst S/N for the $\tau_d = 70$ s case, and attribute this to inadequate background modeling. For all three profile shapes, the size of the uncertainties δT_{90} and δT_{50} were inversely proportional to the burst S/N.

We examined the measured values of T_{90} (T_{50}) for the ensemble of simulated weak (S/N = 5.5 σ) time profiles. A systematic dependence of T_{90} (T_{50}) might reveal itself as a tendency of either measured value to be larger or shorter than the analytic value, The results were consistent with some degree of dependence of T_{90} (T_{50}) on burst S/N for some profile shapes.

We studied the effect of including weak source flux in the user-defined background intervals. Using our worst known case (FRED profiles with τ_d of 70 s), we found that the nearer the background intervals were to the source emission, the larger the deviation of the measured value of T_{90} (T_{50}) was from those calculated analytically. The degree to which the measurements were affected was essentially iden-

© American Astronomical Society • Provided by the NASA Astrophysics Data System

1996ApJ...463..570K

tical for both strong (S/N = 50 σ) and weak (S/N = 5.5 σ) profiles. However, it was observed that the background intervals could also be too far removed from the event, thus not providing enough constraint on the polynomial fit. This is particularly true when using higher order polynominals to fit small background intervals (limited due to the finite time coverage of a data file) separated by large intervals of source flux. This will produce large systematic errors for low fluence events.

We randomly selected 10 background models from those used in the 2B catalog and combined each model with the same simulated burst. Using strong and weak realizations of two profile shapes (triangular and FRED), we concluded that systematic trends in the measured values due to different background models are not observed.

Finally, we utilized burst profiles observed with BATSE to determine the dependence of T_{90} (T_{50}) on the detailed shape of the burst time profile. The signal-to-noise ratios of these profiles were reduced to various levels, and we examined how the measurements changed as a function of S/N for each profile shape. As with the simulated time profiles to which noise had been added, we found that the size of the uncertainties δT_{90} and δT_{50} are inversely proportional to the burst S/N. Only one burst (3B 940206), consisting of a single pulse surrounded by weak extended emission on both sides, exhibited a systematic behavior; this behavior was similar to that observed for the simulated FREDs (see Figs. 7*c* and 7*d*) in which the source flux varied on the same timescale as the background, The other selected bursts showed no evidence for a systematic dependence of T_{90} (T_{50}) on the burst S/N. In addition, we found the changes in T_{90} (T_{50}) induced by a reduction in S/N depended on the detailed shape of the time profile near the times τ_f; in some cases, T_{90} was less sensitive to a reduction of the S/N than T_{50}.

We have distinguished between parent and selected distributions of intrinsic and extrinsic T_{90} s (T_{50} s). The only distribution that is observed is the selected distribution of extrinsic T_{90} s. Some of the factors that shape this distribution are discussed. The selected distribution of extrinsic T_{90} s as observed with BATSE was presented and compared to previously reported observations made with other GRB experiments. The deficiency of bursts at $T_{90} \approx 2$ s in the BATSE-selected distribution of extrinsic T_{90} s is well above the instrument's largest trigger timescale (1.024 s) and it is unlikely a result of the effects of flux-completeness.

We thank John Horack of NASA/MSFC and Robert Mallozzi of the University of Alabama in Huntsville for numerous helpful discussions and for comments on an early version of this manuscript.

APPENDIX A

BATSE INSTRUMENTATION AND DATA TYPES

BATSE consists of eight detector modules mounted on the eight corners of the *CGRO* spacecraft in such a way as to provide near all-sky coverage. There are two gamma-ray detectors within each module, a Large Area Detector (LAD) and a Spectroscopy Detector (SD). The LAD, an uncollimated NaI(Tl) scintillation detector with a surface area of $\sim$2025 cm^2, is optimized for sensitivity over the energy range $\sim$20 keV–2 MeV with modest energy resolution. This study does not use SD data, and thus the SD will not be discussed further.

BATSE sorts the observed counts into four discriminator energy channels every 64 ms. The energy ranges of these four channels are approximately 20–50 keV, 50–100 keV, 100–300 keV, and the last channel is an overflow channel with a lower threshold of $\sim$300 keV. The discriminator data, summed over the energy range 50–300 keV (channels 2 and 3), are continuously monitored for the satisfaction of a set of criteria, upon which a burst trigger is declared. These criteria include a 5.5 σ increase above background simultaneously in two or more detectors, on at least one of three timescales (64, 256, and 1024 ms). When these criteria are satisfied, the instrument enters the burst acquisition mode whereby various burst data types are accumulated and stored in memory, waiting for future readout.

The data types used in this study are the preburst (PREB), the discriminator science (DISCSC), the large area discriminator (DISCLA) data, and the time-tagged event (TTE) data. Each of these data types consist of count rates in four discriminator energy channels. The PREB data cover the 2.048 s prior to the burst trigger time τ_{trg}. The DISCSC data start at τ_{trg} and last for $\sim$240 s prior to 1992 December 17, and for $\sim$550 s thereafter. The time resolution of the PREB and DISCSC data types is 64 ms. The DISCLA data are always available, except during times of *CGRO* telemetry gaps, and have a time resolution of 1.024 s.

While not in a burst acquisition or data readout mode, the TTE data (consisting of the time of arrival and energy channel of each interacting photon) are continuously being recorded in a ring buffer memory of fixed size. Once a burst trigger is set, the most recent $\frac{1}{4}$ of the TTE memory are stored and the remaining memory is filled as the data are accumulated. Thus, the start time of the TTE data is dependent on the burst intensity just prior to the burst trigger time, and the end time of the TTE data depends on how fast the memory is filled after the trigger time. The intrinsic time resolution of TTE data is 2 μs, but these data are summed to a time resolution of 1 ms for the T_{90} calculations.

As with the DISCLA data, due to telemetry gaps the PREB, DISCSC, and TTE data types may not be available for all bursts. In addition, TTE data are not available for those bursts that are overwrites. An overwrite burst is a burst that triggers the instrument while it is still in the burst acquisition or data readout mode. Once the burst trigger is set, the 64 ms trigger threshold is adjusted such that only a burst stronger than the current trigger is allowed to retrigger the instrument. The 256 and 1024 ms thresholds are disabled during burst acquisition and the subsequent data readout. Once the burst trigger is set and the TTE memory are filled, the writing of TTE data to memory is halted and not restarted until after the data readout is over. Therefore the TTE data associated with an overwrite burst (occurring before the accumulation of TTE is restarted) will belong to the previous burst. Lack of TTE data affects only short duration bursts whose time histories are not well resolved with the 64 ms data resulting in large relative errors in the T_{90} (T_{50}) measurements.

© American Astronomical Society • Provided by the NASA Astrophysics Data System

1996ApJ...463..570K

APPENDIX B

ANALYTIC CALCULATIONS OF T_{90} AND T_{50} FOR THREE SIMPLE TIME PROFILES

The simple forms of equations (20), (23), and (24) allow the values of T_{90} and T_{50} to be calculated analytically using equations (2), (3), and (4). For rectangular bursts, represented by equation (23), equation (2) becomes

$$\frac{f}{100} = \frac{\int_{\tau_s}^{\tau_f} P\,dt}{\int_{\tau_s}^{\tau_e} P\,dt}, \tag{36}$$

where P is the peak source count rate summed over all energy channels. Solving for τ_f gives

$$\tau_f = T_d\left(\frac{f}{100}\right) + \tau_s, \tag{37}$$

where the duration $T_d = \tau_e - \tau_s$. Using equations (3) and (4) we find that for simple rectangular burst profiles,

$$T_{90} = 0.9T_d \quad \text{and} \quad T_{50} = 0.5T_d. \tag{38}$$

The analytic values of T_{90} (T_{50}) for the FRED bursts, which are represented by equation (24), can also be calculated straightforwardly. Equation (2) is solved for τ_f, giving

$$\tau_f = \tau_s - \tau_d \ln(1 - f/100). \tag{39}$$

Equations (3) and (4) result in

$$T_{90} = \tau_d \ln(95/5) \quad \text{and} \quad T_{50} = \tau_d \ln(75/25). \tag{40}$$

Analytically calculating the values for T_{90} (T_{50}) of triangular bursts, represented by equation (20), is slightly complicated by the discontinuity at the peak time $\tau_{\rm pk}$. Using equation (1), the total source counts $S_{\rm tot}$ is given by

$$S_{\rm tot} = \tfrac{1}{2}(m - n)\tau_{\rm pk}^2 - \tfrac{1}{2}m\tau_s^2 + \tfrac{1}{2}n\tau_e^2 + (b - d)\tau_{\rm pk} + \tau_e d - \tau_s b, \tag{41}$$

where m, n, b, and d are given by equations (21) and (22). For a simple triangular burst, the exact analytic form of τ_f depends on the size of f relative to the fraction $f_{\rm pk}$ of the total source counts $S_{\rm tot}$ that have been observed by the time $t = \tau_{\rm pk}$.

If $f \le f_{\rm pk}$ then $\tau_f \le \tau_{\rm pk}$ and equation (2) becomes

$$\frac{f}{100} = \frac{\int_{\tau_s}^{\tau_f} (mt + b)dt}{S_{\rm tot}}. \tag{42}$$

This gives a quadratic equation for τ_f,

$$\tfrac{1}{2}m\tau_f^2 + b\tau_f - g = 0, \tag{43}$$

where g is a constant given by

$$g = \frac{1}{2}m\tau_s^2 + b\tau_s + \frac{f}{100}S_{\rm tot}. \tag{44}$$

The correct root t_f of the quadratic equation is determined by a set of physical constraints on τ_f. This equation is valid for $f \le f_{\rm pk}$, giving the first constraints $\tau_s < \tau_f \le \tau_{\rm pk}$. Additional constraints are provided by the set of conditions $\tau_5 < \tau_{25} < \tau_{75} < \tau_{95}$.

If $f > f_{\rm pk}$ then $\tau_f > \tau_{\rm pk}$ and equation (2) becomes

$$\frac{f}{100} = \frac{\int_{\tau_s}^{\tau_{\rm pk}} (mt + b)dt + \int_{\tau_{\rm pk}}^{\tau_f} (nt + d)dt}{S_{\rm tot}}. \tag{45}$$

This gives a different quadratic equation for τ_f,

$$\tfrac{1}{2}n\tau_f^2 + \tau_f d + h = 0, \tag{46}$$

where h is a constant given by

$$h = \tfrac{1}{2}m(\tau_{\rm pk}^2 - \tau_s^2) + b(\tau_{\rm pk} - \tau_s) - \tfrac{1}{2}n\tau_{\rm pk}^2 - \tau_{\rm pk} d - \frac{f}{100}S_{\rm tot}. \tag{47}$$

The correct root t_f is again determined by a set of physical constraints on τ_f. This equation is valid for $f > f_{\rm pk}$, giving the first constraint $\tau_{\rm pk} < \tau_f < \tau_e$. The additional constraints are again provided by the set of conditions $\tau_5 < \tau_{25} < \tau_{75} < \tau_{95}$.

T_{90} and T_{50} are calculated as before using equations (3) and (4), and the equations (43) and (46) for τ_f. Because of the dependence of the form of τ_f on its position relative to $\tau_{\rm pk}$, no simplified expression of either T_{90} (T_{50}) can be obtained for the simple triangular bursts.

© American Astronomical Society • Provided by the NASA Astrophysics Data System

1996ApJ...463..570K

REFERENCES

Begelman, M. C., et al. 1993, MNRAS, 265, L13
Dar, A., et al. 1992, ApJ, 388, 164
Dezalay, J.-P., et al. 1992, in Proc. Huntsville Gamma-Ray Burst Workshop, ed. W. S. Paciesas & G. J. Fishman (Conf. Proc. 265), 304
Fishman, G. J., et al. 1989, in Proc. of the GRO Science Workshop, ed. W. N. Johnson (Greenbelt: NASA/GSFC), 2–39
———. 1994, ApJS, 92, 229
Fishman, G. J., & Meegan, C. A. 1995, ARA&R, 33, 415
Horack, J. M. 1991, NASA Ref. Publ. 1268
Hurley, K. 1992, in Proc. Huntsville Gamma-Ray Burst Workshop, ed. W. S. Paciesas & G. J. Fishman (AIP. Conf. Proc. 265), 3
Kargatis, V. E., et al. 1994, ApJ, 421, L83
Katz, J. I. 1994, ApJ, 422, 248
Klebesadel, R. W., Strong, I. B., & Olson, R. S. 1973, ApJ, 182, L85
Kouveliotou, C., et al. 1991, in Compton Observatory Science Workshop, ed. C. Shrader, N. Gehrels, & B. Dennis (NASA CP-3137), 61
Kouveliotou, C., et al. 1993, ApJ, 413, L101
Meszaros, P., & Rees, M. J. 1993, ApJ, 405, 278
Meegan, C. A., et al. 1994, electronic catalog available from grossc.gsfc.nasa.gov, username gronews, the BATSE 2B Gamma-Ray Burst Catalog
———. 1995, in preparation
Press, W., Flannery, B., Teukolsky, S., & Vetterling, W. 1986, Numerical Recipes (Cambridge: Cambridge Univ. Press)
Rees, M. J., & Meszaros, P. 1992, MNRAS, 258, 41P
Terekhov, O. V., et al. 1994, Astrophys. Lett., 20, 265
———. 1995, Astrophys. Lett., 21, 73
Usov, V. V. 1992, Nature, 357, 472
Weinberg, S. 1972, Gravitation and Cosmology (New York: Wiley)
Woosley, S. E. 1993, ApJ, 405, 273

© American Astronomical Society • Provided by the NASA Astrophysics Data System